



1           Understanding the Optical Properties of Ambient  
2           Sub- and Supermicron Particulate Matter: Results from  
3           the CARES 2010 Field Study in Northern California

4           Christopher D. Cappa<sup>1,\*</sup>, Katheryn R. Kolesar<sup>1,+</sup>, Xiaolu Zhang<sup>1</sup>, Dean B. Atkinson<sup>2</sup>, Mikhail S. Pekour<sup>3</sup>,  
5           Rahul A. Zaveri<sup>3</sup>, Alla Zelenyuk-Imre<sup>3</sup>, Qi Zhang<sup>4</sup>

6           <sup>1</sup> Department of Civil and Environmental Engineering, University of California, Davis, CA 95616, USA

7           <sup>2</sup> Department of Chemistry, Portland State University, Portland, OR, 92707, USA

8           <sup>3</sup> Atmospheric Sciences & Global Change Division, Pacific Northwest National Laboratory, Richland,  
9           WA, 99352, USA

10          <sup>4</sup> Department of Environmental Toxicology, University of California, Davis, CA 95616, USA

11          <sup>+</sup> Now at Department of Chemistry, University of Michigan, Ann Arbor, MI 48109, USA

12          \*Correspondence to: Christopher D. Cappa ([cdcappa@ucdavis.edu](mailto:cdcappa@ucdavis.edu))

### 13           **Short Summary**

14           One way in which particles impact the solar radiation budget is through absorption and scattering  
15           of solar radiation. Here, we report on measurements of aerosol optical properties at visible wavelengths  
16           in the Sacramento, CA region and characterize their relationships with and dependence upon particle  
17           composition, particle size, photochemical ageing, water uptake and heating.

### 18           **Abstract**

19           Measurements of the optical properties (absorption, scattering and extinction) of PM<sub>1</sub>, PM<sub>2.5</sub> and  
20           PM<sub>10</sub> made at two sites around Sacramento, CA during the June 2010 Carbonaceous Aerosols and  
21           Radiative Effects Study (CARES) are reported. These observations are used to establish relationships



22 between various intensive optical properties and to derive information about the dependence of the optical  
23 properties on photochemical ageing and sources. Supermicron particles contributed substantially to the  
24 total light scattering at both sites, about 50% on average. A strong, linear relationship is observed between  
25 the scattering Ångstrom exponent for PM<sub>10</sub> and the fraction of the scattering that is contributed by  
26 submicron particles ( $f_{\text{sca,PM1}}$ ) at both sites and with similar slopes and intercepts (for a given pair of  
27 wavelengths), suggesting that the derived relationship may be generally applicable for understanding  
28 variations in particle size distributions from remote sensing measurements. At the more urban T0 site, the  
29  $f_{\text{sca,PM1}}$  increased with photochemical age whereas at the downwind, more rural T1 site the  $f_{\text{sca,PM1}}$   
30 decreased slightly with photochemical age. This difference in behavior reflects differences in transport,  
31 local production and local emission of supermicron particles between the sites. Light absorption is  
32 dominated by submicron particles, but there is some absorption by supermicron particles (~15% of  
33 the total). The supermicron absorption derives from a combination of black carbon that has penetrated  
34 into the supermicron mode and from dust, and there is a clear increase in the mass absorption coefficient  
35 of just the supermicron particles with increasing average particle size. The mass scattering coefficient  
36 (MSC) for the supermicron particles was directly observed to vary inversely with the average particle  
37 size, demonstrating that MSC cannot always be treated as a constant in estimating mass concentrations  
38 from scattering measurements, or vice versa. The total particle backscatter fraction exhibited some  
39 dependence upon the relative abundance of sub- versus supermicron particles, however this was  
40 modulated by variations in the median size of particles within a given size range; variations in the  
41 submicron size distribution had a particularly large influence on the observed backscatter efficiency and  
42 an approximate method to account for this variability is introduced. The relationship between the  
43 absorption and scattering Ångstrom exponents is examined and used to update a previously suggested  
44 particle classification scheme. Differences in composition led to differences in the sensitivity of PM<sub>2.5</sub> to  
45 heating in a thermodenuder to the average particle size, with more extensive evaporation (observed as a  
46 larger decrease in the PM<sub>2.5</sub> extinction coefficient) corresponding to smaller particles, i.e. submicron  
47 particles were generally more susceptible to heating than the supermicron particles. The influence of  
48 heating on the particle hygroscopicity varied with the effective particle size, with larger changes observed  
49 when the PM<sub>2.5</sub> distribution was dominated by smaller particles.

50



## 51 1. Introduction

52 Atmospheric aerosol particles impact regional and global climate by scattering and absorbing solar  
53 radiation, as well as by affecting the properties of clouds, although the magnitude of these impacts remain  
54 uncertain (IPCC, 2013). The specific ability of particles to interact with solar radiation is dependent upon  
55 particle size, morphology and composition (Bohren and Huffman, 1983), which are often linked through  
56 variations in sources and chemical processing. Atmospheric particles span a wide range of sizes, from just  
57 a few nm to many microns. Quantitative understanding of the absolute and relative contributions across  
58 this entire size range is necessary to assess their climate impacts (Schwartz, 1996). The major sources of  
59 particles within the submicron and supermicron size regimes differ, with submicron particles generally  
60 deriving from combustion emissions and secondary formation and supermicron particles generally  
61 coming from mechanical action (e.g. wind-blown dust or ocean wave breaking) (Seinfeld and Pandis,  
62 1998). As such, particle composition varies across this size range, as does the effectiveness with which  
63 particles absorb and scatter solar radiation. *In situ* measurements of the wavelength- and size-dependent  
64 light scattering and absorption properties of ambient atmospheric particles made concurrent with  
65 measurements of the size-dependent particle composition can provide insights into the impacts of particles  
66 on local climate and air quality (Anderson et al., 2003; Jung et al., 2009), as well as into the more general  
67 relationships between particle size, composition and radiative effects that determine their global impacts  
68 (Quinn et al., 2004; Bates et al., 2006; Wang et al., 2007; Garland et al., 2008; Gyawali et al., 2009; Yang  
69 et al., 2009). Such *in situ* measurements can help to interpret observations from remote sensing (Russell  
70 et al., 2010; Giles et al., 2012) and to provide observational constraints for results from simulations using  
71 regional and global models (Kaufman et al., 2002; Myhre et al., 2012; Tsigaridis et al., 2014).

72 The US Department of Energy Carbonaceous Aerosols and Radiative Effects Study (CARES) took  
73 place in June 2010 with a motivation of improving our understanding of aerosol optical properties and  
74 how they evolve in the atmosphere through observations (Zaveri et al., 2012). Two heavily-instrumented  
75 ground observational sites were set up, one within the greater Sacramento, CA urban area and one  
76 approximately 40 km to the northeast in much more rural Cool, CA (Figure S1). At both sites a variety of  
77 aerosol particle physical, chemical and optical property measurements were made. These two sites were  
78 chosen because of the generally reproducible wind patterns that, much of the time, bring air up from the  
79 San Francisco Bay Area (~100 mi SW) and past the Sacramento urban core before continuing up towards  
80 the foothills of the Sierra Nevada mountains where the air mass accumulates biogenic emissions during  
81 the day, with a reversed flow at night bringing more biogenically influenced air down from the mountains.  
82 In this way, comparison between the two sites facilitates understanding of the role that atmospheric



83 photochemical processing plays in altering particle optical properties. Results from measurements of dry  
84 particle light scattering and absorption made for submicron particulate matter ( $PM_1$ ) and for PM smaller  
85 than  $10\ \mu\text{m}$  ( $PM_{10}$ ) at both sites and of dry particle light absorption and extinction for PM smaller than  
86  $2.5\ \mu\text{m}$  ( $PM_{2.5}$ ) at just the urban Sacramento site are reported in this study. The separate  $PM_1$  and  $PM_{10}$   
87 measurements allows for determination of the optical properties of both submicron and supermicron (PM  
88  $> 1\ \mu\text{m}$ ) particles. The distinct sub- and supermicron measurements are used here to characterize and  
89 examine the variability in their relative contributions as well as the differences between their properties  
90 and sources in the summertime Sacramento region. These regional results are also used to develop more  
91 general understanding of the size- and composition-dependent variability in aerosol particle optical  
92 properties. The analysis here focuses especially on quantifying and assessing the relationships between  
93 various intensive optical parameters (such as the scattering Ångström exponent, the absorption Ångström  
94 exponent, and the single scatter albedo) or between these parameters and characteristics of the particle  
95 distribution (such as the fine mode fraction or characteristic particle diameter) and how these differ  
96 between size ranges (sub- versus supermicron) or are influenced by photochemical ageing or heating.

## 97 **2. Experimental**

98 All measurements were made during the 2010 CARES study, which took place in the Sacramento,  
99 CA region from 2-29 June, 2010. Measurements were made at one of two sites: one located in the greater  
100 Sacramento urban region (termed the T0 site) and one located ca. 40 km northeast downwind in Cool, CA  
101 (termed the T1 site), shown in Figure S1. The CARES study has previously been described in detail (Fast  
102 et al., 2012; Zaveri et al., 2012), and only a brief overview is given here. A list of instrumentation used in  
103 this study is given in Table 1.

### 104 **2.1 Measurements at the T0 Site**

105 Particle light absorption coefficients ( $b_{\text{abs}}$ ) were measured using the UC Davis (UCD) photoacoustic  
106 spectrometer (PAS) at 405 nm and 532 nm (Lack et al., 2012) and using a particle soot absorption  
107 photometer (PSAP; Radiance Research, Inc.) at 470 nm, 532 nm and 660 nm (Bond et al., 1999; Virkkula  
108 et al., 2005). The PAS measured light absorption for  $PM_{2.5}$  sampled through a cyclone, alternating on a  
109 2.5 or 5 minute time scale between bypass measurements (i.e. dried ambient particles) and measurements  
110 behind a constant-temperature ( $225^\circ\text{C}$ ) thermodenuder (Huffman et al., 2008; Cappa et al., 2012) with a  
111 residence time of 5 s. The PAS was calibrated before, during and after the study by referencing the  
112 observed photoacoustic response to added ozone to the extinction measured at the same wavelengths via  
113 cavity ringdown spectroscopy (CRDS) (Lack et al., 2012). The PSAP measured  $b_{\text{abs}}$  for  $PM_1$  or  $PM_{10}$  on



114 an alternating 6 minute cycle. The PSAP was corrected for spot size, flow and particle scattering using  
115 standard methods (Bond et al., 1999; Ogren, 2010). Light scattering and backscattering coefficients ( $b_{\text{sca}}$   
116 and  $b_{\text{bsca}}$ , respectively) were measured for dried particles using a three-wavelength total/backscatter  
117 nephelometer (TSI, Model 3563) at 450 nm, 550 nm and 700 nm. The nephelometer sampled PM<sub>1</sub> and  
118 PM<sub>10</sub> on the same alternating 6 minute cycle as the PSAP. The  $b_{\text{sca}}$  and  $b_{\text{bsca}}$  were corrected for truncation  
119 error (Anderson and Ogren, 1998). Light extinction coefficients ( $b_{\text{ext}} = b_{\text{abs}} + b_{\text{sca}}$ ) were directly measured  
120 for PM<sub>2.5</sub> using the UCD aerosol CRDS (Langridge et al., 2011; Cappa et al., 2012). The  $b_{\text{ext}}$  were  
121 measured for dried particles at both 405 nm and 532 nm, and at 532 nm measurements were additionally  
122 made for particles exposed to elevated RH (~85%). As with the UCD PAS, the CRDS operated behind a  
123 thermodenuder on a 2.5 or 5 minute cycle. PSAP and nephelometer measurements were made over the  
124 period 3-28 June, 2010, with a data gap from the period 16-20 June. The CRD measurements and PAS  
125 measurements at 405 nm were made starting 20:00 PDT on 16 June through 09:00 PDT on 29 June. Due  
126 to a laser malfunction, the PAS measurements at 532 nm started at 12:00 PDT on 19 June. The  
127 thermodenuder measurements began at 12:00 PDT on 20 June.

128 Particle mobility diameter ( $d_{\text{p,m}}$ ) size distributions from 12.2 to 736.5 nm were measured using a  
129 scanning mobility particle sizer (SMPS). Particle aerodynamic diameter ( $d_{\text{p,a}}$ ) size distributions from 542  
130 nm to 19,810 nm were measured using an aerodynamic particle sizer (APS). The APS size distributions  
131 were converted to mobility-equivalent size distributions, assuming spherical particles and a particle  
132 material density of 2.0 g cm<sup>-3</sup> and accounting for the Cunningham slip correction. The use of a material  
133 density of 2.0 g cm<sup>-3</sup> implicitly assumes that the larger particles characterized by the APS were primarily  
134 dust or sea spray. The resulting APS distribution was merged with the SMPS distribution to generate a  
135 time-series of the mobility size distributions with sizes over the entire range (12.2-19,810 nm). Because  
136 the PM<sub>1</sub>, PM<sub>2.5</sub> and PM<sub>10</sub> designations are associated with aerodynamic diameters, mobility equivalent  
137 cut-diameters must be determined. The mobility equivalent cut-diameters are (assuming a density of 2 g  
138 cm<sup>-3</sup>) 700 nm, 1750 nm and 7200 nm, respectively. (For simplicity, we will continue to refer to the sub  
139 and supermicron particle ranges based on the aerodynamic size.) The merged size distribution was  
140 truncated to an upper limit of 7200 nm, and the campaign average for the T0 site is shown for reference  
141 in Figure S2. One complication at the T0 site is that the APS did not collect data from 13:30 PDT on June  
142 22 onwards, and thus information about the supermicron particle size distribution and mass concentrations  
143 are not available after this date.

144 Particle composition was monitored at T0 using the single particle laser ablation time-of-flight mass  
145 spectrometer (SPLAT-II) from 3-28 June (Zelenyuk et al., 2009). SPLAT-II characterizes the composition



146 of individual particles and can be used to build a statistical picture of the distribution of particle types, as  
147 defined by the uniqueness of and similarities between their mass spectra (Zelenyuk et al., 2008). Analysis  
148 of the single particle mass spectra from SPLAT-II indicate a diversity of particle types, including dust,  
149 sea salt-containing (SS), combustion derived (including particles categorized as soot, biomass burning  
150 (BB), primary organic (POA) and hydrocarbon (HC)), amine-containing, and mixed sulfate/organic.  
151 SPLAT-II samples particles between ~50 nm and 2  $\mu\text{m}$ , although the sampling efficiency varies with  
152 particle size and with particle shape. SPLAT-II is optimized for particles with vacuum aerodynamic  
153 diameters ( $d_{va}$ ) between 100 and 600 nm, and detects larger particles with reduced relative efficiency.

154 Non-refractory submicron particle matter (NR-PM) composition was measured using an Aerodyne  
155 high resolution time-of-flight aerosol mass spectrometer (HR-AMS) (Canagaratna et al., 2007). The NR-  
156 PM components measured include organics, sulfate, nitrate, ammonium and chloride. Data during the first  
157 week of the campaign (June 3-12) are especially noisy due to instrumental problems. The AMS data were  
158 processed and NR-PM concentrations determined using standard methods, assuming a collection  
159 efficiency of 50%. Positive matrix factorization was applied to the dataset (Zhang et al., 2011) and three  
160 factors associated with the organic aerosol (OA) were determined. One of these was characterized as a  
161 more-oxidized OA factor (OOA) while two were characterized as less-oxidized OA factors, which will  
162 be referred to here as the hydrocarbon-like OA factor (HOA) and were most likely cooking- and traffic-  
163 related (Atkinson et al., 2015). Black carbon mass concentrations were measured with a single particle  
164 soot photometer (SP2; DMT) (Schwarz et al., 2006). The SP2 was calibrated using mobility size selected  
165 Aquadag particles, using a size-dependent particle density (Gysel et al., 2011). The reported  
166 concentrations have been multiplied by a factor of 1.53 to account for the difference in sensitivity of the  
167 SP2 to Aquadag compared with fullerene soot (R. Subramanian, Personal Communication), which is  
168 thought to be a reasonable proxy for diesel soot (Laborde et al., 2012a). The CARES SP2 instruments  
169 measured BC-containing particles with volume equivalent core diameters between 30 and 400 nm,  
170 although quantification below  $d_{p,ved} < \sim 100$  nm becomes generally more challenging and can vary between  
171 instruments (Laborde et al., 2012b). No adjustment of the reported concentrations for black carbon  
172 containing particles outside of the SP2 detection size range has been made, thus the reported  
173 concentrations may be underestimated (Cappa et al., 2014).

174 Gas-phase concentrations of the sum of NO and NO<sub>2</sub> (= NO<sub>x</sub>) and the sum of nitrogen oxides (= NO<sub>y</sub>) were measured using a 2-channel chemiluminescence instrument (Air Quality Design, Inc.) in which  
175 NO<sub>2</sub> is photolyzed to NO and NO<sub>y</sub> is converted to NO on a Mo catalyst. Gas-phase concentrations of  
176 hydrocarbons, in particular of toluene and benzene, were measured using a proton transfer reaction mass  
177



178 spectrometer (PTR-MS). These measurements can be used to estimate the average photochemical age  
179 (*PCA*) of the air mass (Roberts et al., 1984), with:

180

$$181 \quad PCA_{NO_x} = -\frac{1}{k_{rxn}[OH]} \ln\left(\frac{[NO_x]}{[NO_y]}\right) \quad (1)$$

182 where  $k_{rxn}$  is the reaction rate coefficient for the OH + NO<sub>2</sub> reaction ( $7.9 \times 10^{-12}$  cm<sup>3</sup> molecules<sup>-1</sup> s<sup>-1</sup>;  
183 (Brown et al., 1999)), and

184

$$185 \quad PCA_{HC} = \frac{\ln(ER) - \ln\left(\frac{[benzene]}{[toluene]}\right)}{(k_b - k_t)[OH]} \quad (2)$$

186

187 where *ER* is the emission ratio between benzene and toluene, assumed here to be 3.2 (Warneke et al.,  
188 2007), and  $k_b$  and  $k_t$  are the reaction rate coefficients for reaction of benzene ( $1 \times 10^{-12}$  cm<sup>3</sup> molecule<sup>-1</sup> s<sup>-1</sup>)  
189 and toluene ( $5.7 \times 10^{-12}$  cm<sup>3</sup> molecule<sup>-1</sup> s<sup>-1</sup>) with OH, respectively (Atkinson et al., 2006). Although there  
190 are challenges in interpreting *PCA* estimates quantitatively due to e.g. mixing of different sources (Parrish  
191 et al., 2007) and weekend/weekday differences (Warneke et al., 2013), *PCA* nonetheless provides a useful  
192 estimate of the extent of photochemical processing.

## 193 **2.2. Measurements at the T1 Site**

194 A similar suite of measurements were made at the T1 site as at the T0 site, including light absorption  
195 at 470, 532, 660 nm by PSAP, light scattering at 450, 550, 700 nm by nephelometer, particle size by  
196 SMPS and APS and submicron particle composition by HR-AMS and SP2. The SMPS deployed at T1  
197 measures particle number distribution in the range of 10 – 858 nm in  $d_{p,m}$ . Analysis of the HR-AMS data  
198 using positive matrix factorization identified two distinct OOA factors, one of which was mainly  
199 associated with biogenic emissions and the other representative of secondary organic aerosol (SOA)  
200 formed in photochemically processed urban emissions. HOA was also observed at T1 but it on average  
201 accounted for only ~10% of the OA mass. Details on HR-AMS and SMPS measurements at T1 and  
202 associated data analysis are given in (Setyan et al., 2012; Setyan et al., 2014). The particle scattering and  
203 absorption measurements were made nearly continuously from 3-28 June, 2010. Light absorption  
204 measurements were also made using different PAS instruments, although these are not utilized here.  
205 PTR-MS measurements of toluene and benzene are available from 3-28 June, 2010. Although NO and



206 NO<sub>y</sub> measurements were made, NO<sub>x</sub> was not measured. Thus, it is only possible to estimate *PCA* at the  
207 T1 site using the benzene-toluene method (Equation 2).

208 One additional way in which particle composition was characterized at T1 was with a particle  
209 ablation laser-desorption mass spectrometer (PALMS) (Cziczo et al., 2006). The PALMS is similar to the  
210 SPLAT-II in that single particle mass spectra are collected for particles between about  $d_{p,a}$  150 nm and 2  
211 μm, which are used to build a statistical picture of particle types. Analysis of the single particle mass  
212 spectra from PALMS at the T1 site yielded the following particle types: dust (termed MinMet for  
213 mineralogical/meteoritic), sea salt-containing (SS), combustion derived (including particles categorized as  
214 soot, biomass burning (BB), or oil), mixed sulfate/organic and “other.” Results from the PALMS  
215 measurements have been previously reported in Zaveri et al. (2012).

### 216 **2.3 Derived particle properties**

217 Using the alternating (i.e. sequential) PM<sub>1</sub> and PM<sub>10</sub> measurements, the properties of supermicron  
218 particles specifically have been estimated from the difference between PM<sub>10</sub> and PM<sub>1</sub>, with

$$219 \quad b_{x,super} = \frac{b_{x,PM10}(t-1) + b_{x,PM10}(t+1)}{2} - b_{x,PM1}(t) \quad (3)$$

220 where  $x$  indicates absorption or scattering and where the  $t$  values indicate the average concentration over  
221 each 6 min averaging period (i.e. the PM<sub>1</sub>-PM<sub>10</sub> cycle time). The fraction of absorption or scattering from  
222 PM<sub>1</sub> or supermicron PM is therefore defined as:

$$223 \quad f_{x,PM1} = \frac{b_{x,PM1}}{b_{x,PM10}} \quad (4a)$$

$$224 \quad f_{x,super} = \frac{b_{x,super}}{b_{x,PM10}} \quad (4b)$$

225 where  $x$  again indicates absorption or scattering. These ratios give an indication of the contribution of  
226 submicron or supermicron particles to the total absorption or scattering, e.g. larger values of  $f_{sca,PM1}$   
227 indicate greater dominance of the submicron particle mode in terms of total scattering.

228 Light absorption measurements are used to determine the absorption Ångstrom exponent (*AAE*),  
229 which characterizes the wavelength dependence of absorption and is given as:

$$230 \quad AAE_{\lambda1,\lambda2} = -\frac{\log\left(\frac{b_{abs,\lambda1}}{b_{abs,\lambda2}}\right)}{\log\left(\frac{\lambda1}{\lambda2}\right)} \quad (5)$$



231 where  $\lambda_1$  and  $\lambda_2$  indicate different wavelengths. It is often assumed that “pure” black carbon (BC)  
 232 particles have an *AAE* close to 1 and that values  $>1$  indicate the presence of light absorbing organics  
 233 (referred to as brown carbon, or BrC) or dust, which tend to exhibit absorption that increases sharply as  
 234 wavelength decreases. The *AAE* is dependent upon the chosen wavelength pair. The specific wavelength  
 235 pair used to calculate *AAE* will be indicated using the notation  $AAE_{\lambda_1-\lambda_2}$ . Related, the difference in the  
 236  $PM_{10}$  and  $PM_1$  *AAE* can be calculated:

$$237 \quad \Delta AAE_{10-1} = AAE_{PM_{10}} - AAE_{PM_1} \quad (6)$$

238 The scattering Ångström exponent (*SAE*) is also commonly used to characterize the relative  
 239 contributions from sub- and supermicron particles, and is defined analogously to the *AAE* as:

$$240 \quad SAE_{\lambda_1,\lambda_2} = -\frac{\log\left(\frac{b_{sca,\lambda_1}}{b_{sca,\lambda_2}}\right)}{\log\left(\frac{\lambda_1}{\lambda_2}\right)} \quad (7)$$

241 Larger values of the *SAE* correspond to overall smaller particles, and have been calculated for  $PM_1$ ,  $PM_{10}$   
 242 and  $PM_{super}$ . A similar parameter, the extinction Ångström exponent, *EAE*, can be calculated for  $PM_{2.5}$   
 243 using the measured  $b_{ext}$ .

244 The fraction of extinction due to scattering is characterized through the single scatter albedo (*SSA*),  
 245 which can be written in multiple ways depending on whether  $b_{ext}$ ,  $b_{abs}$  or  $b_{sca}$  were the directly measured  
 246 properties:

$$247 \quad SSA = \frac{b_{ext} - b_{abs}}{b_{ext}} = \frac{b_{sca}}{b_{ext}} = \frac{b_{sca}}{b_{sca} + b_{abs}} \quad (8)$$

248 The angular dependence of scattering is characterized through measurement of the backscatter  
 249 coefficients,  $b_{bsca}$ . The fraction of light that is backscattered, relative to the total scattering, is calculated  
 250 as

$$251 \quad f_{bsca} = \frac{b_{bsca}}{b_{sca}} \quad (9)$$

252 The backscatter fraction is an important climate-relevant parameter as particle radiative effects depend in  
 253 part on the extent to which incoming solar radiation is reflected back to space versus absorbed within the  
 254 Earth system. The backscatter fraction is commonly converted to an asymmetry parameter,  $g_{sca}$ , and the  
 255 empirically derived relationship between these is (Andrews et al., 2006):

$$256 \quad g_{sca} = -7.143889 \cdot f_{bsca}^3 + 7.464439 \cdot f_{bsca}^2 - 3.9356 \cdot f_{bsca} + 0.9893 \quad (10)$$



257 The asymmetry parameter is the intensity-weighted average of the cosine of the scattering angle and  
 258 ranges from -1 (all backscatter) to 1 (all forward scatter).

259 Using the measurements made behind the thermodenuder at the T0 site (i.e. the PAS and CRD  
 260 measurements), various ratios and differences can be determined. The ratio between the denuded and  
 261 undenuded extinction (i.e. the fraction of extinction remaining for PM<sub>2.5</sub>) provides a measure of the  
 262 particle volatility, with smaller values indicating more volatile particles:

$$263 \quad f_{ext,TD} = \frac{b_{ext,TD}}{b_{ext,amb}} = \frac{b_{ext(t-1)} + b_{ext(t+1)}}{2b_{ext(t)}} \quad (11)$$

264 where *TD* indicates the thermodenuded and *amb* indicates the ambient time periods, and the 2<sup>nd</sup> equality  
 265 shows how the sequential TD and ambient measurements were accounted for similar to Eqn. 3. The  
 266 change in particle hygroscopicity upon thermodenuding is calculated as

$$267 \quad \Delta\gamma_{RH} = \gamma_{RH}(amb) - \gamma_{RH}(TD) \quad (12)$$

268 where

$$269 \quad \gamma_{RH} = \log\left(\frac{b_{ext,high}}{b_{ext,low}}\right) / \log\left(\frac{100-RH_{low}}{100-RH_{high}}\right) \quad (13)$$

270 and the *high* and *low* refer to the humidified and dried CRD measurements and again accounting for the  
 271 sequential nature of the *TD* and *amb* measurements. The parameter  $\gamma_{RH}$  can be thought of as the optical  
 272 hygroscopicity (i.e. a measure of the affinity of particles towards water), although it does have some  
 273 dependence on particle size and thus there is not a 1-to-1 relationship between  $\gamma_{RH}$  and particle  
 274 hygroscopicity (Atkinson et al., 2015). In general, for a given amount of particle growth due to water  
 275 uptake,  $\gamma_{RH}$  is larger for smaller particles.

276 The difference in the AAE between the ambient and thermodenuded states can also be determined:

$$277 \quad \Delta AAE_{amb-TD} = AAE_{amb} - AAE_{TD} \quad (14)$$

278 Mass absorption, scattering and extinction coefficients (*MAC*, *MSC* and *MEC*, respectively) have been  
 279 calculated for the various wavelengths and PM size ranges. Using scattering as an example,

$$280 \quad MSC_X \left(\frac{m^2}{g}\right) = \frac{b_{sca}}{[X]} \quad (15)$$

281 where [X] is the mass concentration of the reference species of interest, such as BC or the total PM. In  
 282 the case of [BC], the SP2 measurements are used. For total PM, the integrated volume concentrations



283 were used to estimate [PM], assuming spherical particles. For supermicron particles it was assumed that  
 284  $\rho_p = 2.0 \text{ g cm}^{-3}$  and for submicron particles the density was  $1.3 \text{ g cm}^{-3}$  (Setyan et al., 2012).

285 The size distributions have been used to calculate median surface-weighted particle diameters  
 286 ( $d_{p,\text{surf}}$ ) as:

$$287 \quad d_{p,\text{surf}} = \frac{\int_{d_{p,\text{low}}}^{d_{p,\text{high}}} d_p \frac{dN}{d \log d_p} d \log d_p}{\int_{d_{p,\text{low}}}^{d_{p,\text{high}}} \frac{dN}{d \log d_p} d \log d_p} \quad (16)$$

288 where  $dN/d \log d_p$  is the observed number-weighted size distribution over the size range of interest ( $d_{p,\text{low}}$   
 289 to  $d_{p,\text{high}}$ ). In this study,  $d_{p,\text{surf}}$  values have been separately calculated for the total  $\text{PM}_{10}$  distribution and  
 290 for the supermicron particle range.

## 291 3. Results and Discussion

### 292 3.1 Size dependence of optical properties

#### 293 3.1.1 Light scattering

294 Supermicron particles contributed substantially to the dry particle scattering at both T0 and T1  
 295 (Figure 1). The average  $f_{\text{sca},\text{PM}_{10}}(550 \text{ nm})$  at T0 was  $0.48 \pm 0.17 (1\sigma)$  and at T1 was  $0.55 \pm 0.16 (1\sigma)$ . (If  
 296 the time period where the scattering measurements were not available at T0 is excluded from the T1  
 297 average, the average  $f_{\text{sca},\text{PM}_{10}}$  is  $0.57 \pm 0.15 (1\sigma)$ .) Thus, nearly 50% of the dry scattering at these two sites  
 298 was, on average, due to supermicron particles during the campaign period. This observation is consistent  
 299 with results from Kassianov et al. (2012), who calculated scattering and direct radiative forcing for these  
 300 two sites based on observed size distributions and concluded that supermicron particles contribute  
 301 substantially to the total scattering. Because scattering generally increases more rapidly with decreasing  
 302 wavelength for small particles, the  $f_{\text{sca},\text{PM}_{10}}$  is larger for 450 nm (= 0.59 at T0 and 0.67 at T1) and smaller  
 303 for 700 nm (= 0.34 at T0 and 0.41 at T1) compared to 550 nm. The similarity of the  $f_{\text{sca},\text{PM}_{10}}$  values between  
 304 the two sites is noteworthy given that the T0 site is situated much closer to urban Sacramento than is the  
 305 T1 site. The  $f_{\text{sca},\text{PM}_{10}}$  values at the two sites show a strong, linear correlation with the  $\text{SAE}_{450,550}$  (Figure  
 306 2a,b), which is not entirely surprising since the  $\text{SAE}$  provides an indication of the mean, optically-  
 307 weighted particle size. There is a similarly strong relationship with the  $\text{SAE}$  values calculated from the  
 308 other wavelength pairs (Figure S3 and Figure S4 show results for the T0 and T1 sites, respectively, for  
 309 comparison). The best fit from a one-sided linear fit to  $\text{SAE}_{450,550}$  versus  $f_{\text{sca},\text{PM}_{10}}$  at T0 is  $\text{SAE}_{450,550} = 2.69$



310  $f_{\text{sca},550,\text{PM1}} - 0.05$  ( $r^2 = 0.88$ ) and at T1 is  $SAE_{450,550} = 2.66 f_{\text{sca},550,\text{PM1}} + 0.06$  ( $r^2 = 0.91$ ). (Values for other  
311 combinations of wavelengths for T0 and T1 are reported in Table S1.)

312 Although the  $SAE$  values exhibit a linear relationship with  $f_{\text{sca},\text{PM1}}$ , they exhibit a more complex  
313 relationship with the median surface-area weighted particle diameter of the entire distribution ( $d_{\text{p,surf,PM10}}$ ).  
314 Although the  $SAE$  values generally decrease with increasing  $d_{\text{p,surf,PM10}}$ , as one might expect since an  
315 increase in  $d_{\text{p,surf,PM10}}$  presumably corresponds to an increase in the supermicron fraction of scattering,  
316 there is much greater scatter compared to the clear relationship with  $f_{\text{sca},\text{PM1}}$ , and clear periods when a  
317 monotonic relationship is not observed (Figure 2c,d). The derived  $d_{\text{p,surf,PM10}}$  values are sensitive to the  
318 exact shapes of the sub- and supermicron modes, and the  $MSC$  for supermicron particles, in particular, is  
319 also sensitive to the shape of the supermicron size distribution (discussed further below in Section 3.1.2).  
320 Consequently, there is not a straight-forward relationship between the  $SAE$  and  $d_{\text{p,surf,PM10}}$  and the  $SAE$   
321 cannot be used to predict average properties of the overall sub- plus supermicron size distribution.  
322 However, the strong, linear relationship between the  $SAE$  and  $f_{\text{sca},\text{PM1}}$  and the close correspondence  
323 between the two sites, despite apparent variations in the underlying size distributions, suggests that the  
324 relationships derived here may be sufficiently general to be applied in other locations, although this needs  
325 to be verified. This in turn indicates that observations of  $SAE$  can be used to quantitatively estimate the  
326 fractional contribution of sub and supermicron particles to the total scattering with an uncertainty of ~15%  
327 based on the spread in the data. Thus, the relationships derived here may be useful for application or  
328 comparison with remote sensing methods, such as the AERONET sun photometer network (Schuster et  
329 al., 2006) or satellites (Ginoux et al., 2012).

330 One factor that can influence the sub- versus supermicron contributions to the total scattering is the  
331 extent of photochemical processing. Photochemical processing leads to the production of condensable  
332 material that will tend to condense according to the particle Fuchs-corrected surface area. As such,  
333 photochemical processing and secondary PM formation, especially SOA, will lead to preferential growth  
334 of the submicron mode diameters (which grow more for a given amount of material condensed) and will  
335 lead to an increase in the submicron scattering in particular. The  $f_{\text{sca},\text{PM1}}$  at T0 exhibits a general increase  
336 with PCA (characterized by the  $[\text{NO}_x]/[\text{NO}_y]$  and/or  $[\text{benzene}]/[\text{toluene}]$  ratios), although there is a fair  
337 amount of scatter at low photochemical age (Figure 3a,b). The  $f_{\text{sca},\text{PM1}}$  at T1 shows completely different  
338 behavior, with  $f_{\text{sca},\text{PM1}}$  exhibiting very little dependence on PCA, although there is possibly a slight  
339 decrease (Figure 3c). There is generally good correspondence between the  $[\text{NO}_x]/[\text{NO}_y]$  and  
340  $[\text{benzene}]/[\text{toluene}]$  ratios measured at T0, indicating that the different results at T1 are unlikely to result  
341 from use of a particular PCA marker (Figure 3d). The PCA at T1 is on average much larger than at T0.



342 The PCA at the T0 site exhibits a clear peak around 15:00 PDT (Figure 3e). The PCA diel profile at T1  
343 is comparably much broader and exhibits a less-pronounced peak, but that also occurs in the late afternoon  
344 (around 16:00 PDT) (Figure 3e). This broadening and different temporal dependence likely reflects the  
345 downwind location of the T1 site and the general flow patterns in this region (Fast et al., 2012). It seems  
346 likely that the difference in variation of the  $f_{\text{sca,PM1}}$  with PCA between the two sites is related to these  
347 difference. At T0, the measured  $b_{\text{sca,PM1}}$  may reflect a relatively local production of submicron particulate  
348 mass whereas at T1 the  $b_{\text{sca,PM1}}$  is more reflective of regional conditions. The  $b_{\text{sca,super}}$  at both sites will  
349 have some regional contribution (in particular sea spray), but also a strong local contribution. Wind speeds  
350 were typically largest in the mid- to late afternoon at both sites, although overall the diel behavior was  
351 much clearer at T1 than at T0 and with a larger amplitude (Figure 3e). However, the wind speeds were on  
352 average larger at T0. Thus, it seems reasonable to conclude that local emission of supermicron  
353 particulates, possibly re-suspended road dust or from agricultural sources, in the afternoon at T1  
354 counteracts the influence of growth of the regional submicron particulates, leading  $f_{\text{sca,PM1}}$  to be nearly  
355 independent of PCA at this site. In contrast, at T0 the local photochemical production of new submicron  
356 PM mass appears to be sufficiently strong to lead to an increase in  $f_{\text{sca,PM1}}$  with PCA.

### 357 3.1.2 Light absorption

358 Light absorption at both sites was dominated by submicron particles, although a small fraction may  
359 also be from supermicron particles (Figure 1). The average  $f_{\text{abs,PM1}}$  at 532 nm at T0 was  $0.89 \pm 0.14$  ( $1\sigma$ )  
360 and at T1 was  $0.85 \pm 0.17$  ( $1\sigma$ ). At T1 there is a slight indication that  $f_{\text{abs,super}}$  decreased as  $f_{\text{sca,super}}$   
361 decreased, but no such relationship is clearly evident at T0 (Figure 1g-h). Such potential relationships  
362 must be viewed with some amount of caution, as the PSAP requires correction for particle scattering and  
363 the extent of forward versus backward scattering is particle size dependent. It is also known that the PSAP  
364 shows an additional sensitivity to particle size due to differences in the depth of penetration of particles  
365 into the filter (Nakayama et al., 2010), which might influence the measurements here.

366 That light absorption is dominated by submicron particles suggests that black carbon, and possibly  
367 brown carbon, make up the majority of the light absorbing particle burden. The  $AAE_{\text{PM1}}$  values at both T0  
368 and T1 exhibit reasonably normal distributions (Figure 4). The spread at T0 was substantially smaller than  
369 at T1. The average  $AAE_{\text{PM1}}$  values are slightly larger than unity at both sites ( $1.21 \pm 0.13$  and  $1.33 \pm 0.22$   
370 for T0 and T1, respectively, where uncertainties are 1 standard deviation; Table 2), and do not show any  
371 pronounced dependence on the wavelength pair chosen. Black carbon is typically thought to have an  $AAE$   
372 close to unity (Cross et al., 2010). The average  $\text{PM1 } AAE_{\text{PM1,450-532}}$  are identical between the sites, whereas  
373 the  $AAE_{\text{PM1,450-660}}$  and  $AAE_{\text{PM1,532-660}}$  are slightly larger at T1. The larger spread in the  $AAE_{\text{PM1}}$  values for



374 all wavelength pairs at T1 suggests that the two PSAP instruments were not entirely identical and had  
375 somewhat different noise characteristics, making it difficult to establish whether these small differences  
376 are real. One method that has been used to estimate the contribution of brown carbon relative to black  
377 carbon is to extrapolate the observed  $b_{\text{abs}}$  at longer  $\lambda$  (e.g. 660 nm) to shorter wavelengths assuming that  
378  $AAE = 1$  and that absorption by brown carbon at long  $\lambda$  is zero (Gyawali et al., 2009; Yang et al., 2009;  
379 Chung et al., 2012; Lack and Langridge, 2013). To the extent that this method is appropriate, and some  
380 have argued it may not be (Lack and Langridge, 2013), it provides an estimate of  $b_{\text{abs}}$  for pure BC  
381 (assuming that  $AAE_{\text{BC}} = 1$  exactly) and the contribution from brown carbon can then be estimated by  
382 subtracting the pure BC  $b_{\text{abs}}$  from the total. Given the observed  $AAE_{\text{PM1}}$  values, this spectral differencing  
383 method suggests that brown carbon contributes ~6% at T0 and up to 11% at T1 to submicron particle light  
384 absorption at 450 nm; if the actual  $AAE_{\text{BC}}$  were  $>1$ , as possibly suggested by the  $AAE_{532-660}$  measurements  
385 at both sites, then the attributed brown carbon fraction would be even smaller. These relatively minor  
386 contributions from brown carbon are consistent with the conclusions of Cappa et al. (2012) and indicate  
387 that in this region the summertime submicron particulate light absorption is predominately from black  
388 carbon.

389 There are two likely origins of the supermicron absorption: penetration of BC into the supermicron  
390 size range, likely from coagulation of BC with larger particles or tailing of the predominately submicron  
391 BC size distribution, or dust (assuming the observed supermicron absorption is not simply an experimental  
392 artifact). Dust is known to contribute substantially to the  $\text{PM}_{10}$  burden in Sacramento, with sources  
393 including roadways, agricultural activity and disturbed open residential areas (California Air Resources  
394 Board, 2005; <http://www.arb.ca.gov/pm/pmmeasures/pmch05/pmch05.htm>), as well as long range  
395 transport (Ewing et al., 2010). The single particle measurements from the SPLAT-II instrument at T0  
396 indicate that both BC-containing and dust particles are observed in the supermicron size range, along with  
397 substantial contributions from sea salt-containing particles that are likely of marine origin (Figure S5).  
398 The PALMS instrument detected similar particle types at the T1 site (Zaveri et al., 2012) Although  
399 informative, these measurements unfortunately cannot be used to quantitatively assess the relative  
400 contributions of the different absorbing particle types to the supermicron absorption because both  
401 instruments sample only over a subset of the entire supermicron size range, e.g. the SPLAT-II only up to  
402  $d_{v,a} \sim 2 \mu\text{m}$ . Nonetheless, the single particle composition measurements provide support for the likely  
403 origin of the supermicron absorption being from either BC penetration or dust.

404 Dust and BC should be distinguishable based on the observed spectral properties and chemical  
405 composition. Although the optical properties of dust vary by location and source, dust is generally thought



406 to have  $AAE$  values  $> 1$ , with typical reported values of  $\sim 1.5$ -3 (Yang et al., 2009; Russell et al., 2010;  
407 Bahadur et al., 2012), larger than is typically observed for black carbon. The measured average  $AAE_{\text{super}}$   
408 values were typically greater than unity and larger than the  $AAE_{\text{PM1}}$  (Table 2), suggestive of a dust  
409 influence. However, there are two important points to consider. First, although the  $AAE_{\text{super}}$  values were  
410 approximately normally distributed, the distributions were substantially broader than the distributions for  
411 the submicron particles, with a range of about  $0.5 < AAE_{\text{super}} < 3$  (Figure 4). Second, the  $AAE_{\text{super}}$  values  
412 exhibited a notable wavelength-pair dependence, with the largest values observed for the 450-532 nm pair  
413 and the smallest for the 532-660 nm pair and where the wavelength-dependence at T0 was much larger  
414 than at T1 (Table 2; Figure 4). The large spread in the  $AAE_{\text{super}}$  values may reflect the small magnitudes of  
415 the absolute  $b_{\text{abs,super}}$  values and the use of the difference method to determine the  $b_{\text{abs,super}}$  (i.e. noise), but  
416 could also indicate a greater diversity in  $AAE_{\text{super}}$  values compared to  $AAE_{\text{PM1}}$  due to, perhaps, time-  
417 varying contributions from dust and BC. As a test, if the averaged  $AAE_{\text{PM1}}$  values are restricted to periods  
418 when the absolute absorption was relatively low ( $< 0.6 \text{ Mm}^{-1}$ ), but still generally larger than the  $b_{\text{abs,super}}$ ,  
419 there is no substantial additional broadening of the distribution. This suggests that the broadening of  
420  $AAE_{\text{super}}$  may be real and that the latter interpretation—diversity in individual  $AAE_{\text{super}}$  values—may be  
421 appropriate. However, since there were insufficient periods where the  $b_{\text{abs,PM1}}$  values were as low as the  
422  $b_{\text{abs,super}}$ , changes in the shape of the  $AAE_{\text{PM1}}$  distribution cannot be assessed under the exact same  
423 conditions, and thus the possibility that the greater scatter simply reflects the low  $b_{\text{abs,PM10}}$  values cannot  
424 be ruled out. (The  $0.6 \text{ Mm}^{-1}$  threshold was chosen to allow for a sufficient number of  $AAE_{\text{PM1}}$  values to  
425 remain to be used to develop a histogram.) Also, if one considers the relationship between  $AAE_{\text{PM10}}$  and  
426 the  $f_{\text{sca,PM1}}$ , there is no obvious broadening of the  $AAE$  distribution at smaller values of  $f_{\text{sca,PM1}}$ . There is  
427 also some indication of correlations between both  $b_{\text{abs,super}}$  and  $b_{\text{abs,PM1}}$  and between  $b_{\text{abs,super}}$  and [BC] (as  
428 measured by the SP2) (Figure 5). Although the correlation coefficients are relatively small ( $r^2 = 0.45$  and  
429  $0.25$  at T0 and T1, respectively), this could indicate contributions from penetration of BC into the  
430 supermicron mode, which could help to explain why most of the  $AAE_{\text{super}}$  values are smaller than is typical  
431 for pure dust but larger than for BC.

432 Further insight into the nature of the supermicron particles comes from consideration of the  $MAC$   
433 and  $MSC$  values, which are intensive properties like the  $AAE$ . The  $MAC$  and  $MSC$  for supermicron  
434 particles have been assessed by comparing  $b_{\text{abs,super}}$  and  $b_{\text{sca,super}}$  with the supermicron mass concentration  
435 ( $[PM_{\text{super}}]$ ) as estimated from the measured size distributions (Figure 6a-b). The  $[PM_{\text{super}}]$  values were  
436 estimated assuming a density of  $2 \text{ g cm}^{-3}$  and spherical particles. In theory, the  $MSC$  is size dependent,  
437 falling off rapidly from  $\sim 4 \text{ m}^2 \text{ g}^{-1}$  to  $\sim 1.5 \text{ m}^2 \text{ g}^{-1}$  in going from  $d_{\text{p,m}} = 700$  to  $1000 \text{ nm}$  (with  $d_{\text{p,m}} = 700 \text{ nm}$   
438 corresponding approximately to  $d_{\text{p,a}} = 1000 \text{ nm}$  when density =  $2 \text{ g cm}^{-3}$ ) and ranging from  $\sim 0.5 \text{ m}^2 \text{ g}^{-1}$



439 to  $1.5 \text{ m}^2 \text{ g}^{-1}$  for larger particles (see Figure S6 and (Clarke et al., 2004)). Thus, smaller  $MSC$  values  
440 generally correspond to overall larger particles. The observed  $MSC_{\text{super}}$  exhibit an inverse relationship  
441 with  $d_{\text{p,surf}}$  for the supermicron particles (Figure 6e-f). To our knowledge, this is the first explicit  
442 demonstration of the theoretically expected inverse relationship from ambient observations. These  
443 observations indicate that the nature of the supermicron particle size distributions do vary with time, with  
444 some time periods containing larger supermicron particles and some smaller. This variability in size  
445 suggests variations in the supermicron particle sources, and consequently in the chemical nature of the  
446 particles, discussed further below.

447 The relationship between  $b_{\text{abs,super}}$  and  $[PM_{\text{super}}]$  exhibits a great deal of scatter (Figure 6c-d), most  
448 likely due to the small values of  $b_{\text{abs,super}}$  and to the variability in the  $PM_{\text{super}}$  sources, including particle  
449 density and size. The  $MAC$  values at 532 nm for the supermicron particles range from  $\sim 0$  to  $\sim 0.06 \text{ m}^2 \text{ g}^{-1}$   
450 at both sites. Further, the  $MAC_{\text{super}}$  values exhibit a notable dependence on the  $d_{\text{p,surf}}$  (Figure 6g-h). In  
451 general, when  $d_{\text{p,surf}}$  is on the small side ( $\sim 2 \mu\text{m}$ ) the  $MAC_{\text{super}}$  is very close to zero and it tends to increase  
452 with  $d_{\text{p,surf}}$ . Apparently, the particles from sources that produced, on average, smaller supermicron  
453 particles were less absorbing than the particles from sources that produced larger particles. A plausible  
454 explanation is that the larger particles are dust while the smaller (yet still supermicron) particles are a  
455 combination of non-absorbing sea spray particles and other particle types that are penetrating from the  
456 submicron mode. This hypothesis is generally supported by examination of HYSPLIT back trajectories  
457 (Draxler and Rolph) for each day of the campaign (Figure S7), as well as by comparison with the source-  
458 region identification in Fast et al. (Fast et al., 2012), with smaller  $d_{\text{p,surf}}$  values for the supermicron particles  
459 generally corresponding to periods when the air masses were identified as containing a greater “Bay Area”  
460 contribution. Considering three specific days as examples, two (11 and 16 June) when the  $MSC_{\text{super}}$  were  
461 particularly small (corresponding to larger particles) and one (15 June) when the  $MSC_{\text{super}}$  were larger,  
462 clear differences in the air mass origins can be seen. Specifically, the back trajectories on 11 and 16 June  
463 indicate that the air mass came from almost due north, consistent with a terrestrial origin for the particles  
464 while the back trajectory on 15 June indicates that the air mass had passed over the San Francisco Bay  
465 Area and before that came from along the CA coast. These back trajectories are generally consistent with  
466 the idea that when the overall size distribution is skewed towards smaller supermicron particles (smaller  
467  $d_{\text{p,surf}}$  and larger  $MSC_{\text{super}}$ ) the air masses are more impacted by sea spray particles, while when the size  
468 distribution is skewed towards larger particles there is a greater relative dust contribution.

469 Even though the  $MAC_{\text{super}}$  exhibits a pronounced relationship with  $d_{\text{p,surf}}$ , there is actually minimal  
470 dependence of  $b_{\text{abs,super}}$  on  $d_{\text{p,surf}}$  (Figure S8). There is, however, a relatively strong relationship between



471 [PM<sub>super</sub>] and  $d_{p,surf}$ , with larger [PM<sub>super</sub>] usually corresponding to smaller  $d_{p,surf}$  (Figure S8). This suggests  
472 that the small  $MAC_{super}$  values at small  $d_{p,surf}$  result from substantial inputs of non-absorbing supermicron  
473 particles, which does not necessarily alter the observed  $b_{abs,super}$  but does serve to increase the [PM<sub>super</sub>],  
474 thereby depressing the  $MAC_{super}$  values. The  $MAC_{super}$  is approximately  $0.06 \text{ m}^2 \text{ g}^{-1}$  when  $d_{p,surf}$  is large  
475 (i.e.  $>3.5 \text{ }\mu\text{m}$ ; Figure 6). If it is assumed that the major contributor to supermicron absorption when  $d_{p,surf}$   
476 is large is dust then a value for the imaginary refractive index ( $k$ ) for dust in this region is estimated from  
477 Mie theory. Assuming spherical particles with  $d_p = 3.5 \text{ }\mu\text{m}$  with density =  $2 \text{ g cm}^{-3}$  and a real refractive  
478 index of either 1.5 or 1.6, the  $k$  is  $\sim 0.0035i$ . However, this estimate assumes that all of the PM<sub>super</sub> mass  
479 is dust and that no other absorbing species contribute. If some of the PM<sub>super</sub> mass is attributed to non-  
480 dust species, then the derived dust-specific  $MAC$  and  $k$  would be larger. Alternatively, if BC contributes  
481 substantially to the observed supermicron absorption, which seems likely, then the dust-specific  $MAC$  and  
482  $k$  would be smaller. Most likely, the above values are upper-limits. Despite these uncertainties, the  
483 observed  $MAC$  and  $k$  are similar to reported estimates for dust in the Xianghe area in China, where  $MAC_{dust}$   
484 =  $0.048 \text{ m}^2 \text{ g}^{-1}$  at 520 nm and where the reported  $MAC$  has been adjusted to a density of  $2.0 \text{ g cm}^{-3}$  (Yang  
485 et al., 2009). Overall, although the contribution of supermicron particles to the total absorption is small in  
486 this region, it nonetheless must be considered.

### 487 3.1.3 Relationship between scattering and absorption

488 There has been increasing interest in the relationship between the absorption Ångstrom exponent  
489 and the scattering Ångstrom exponent (Yang et al., 2009; Russell et al., 2010; Bahadur et al., 2012; Giles  
490 et al., 2012; Cazorla et al., 2013; Costabile et al., 2013). The wide range of  $SAE$  values observed here  
491 allows for assessment of the  $AAE$  vs.  $SAE$  relationship in a constrained environment. The observed  
492  $AAE_{532-660}$  vs.  $SAE_{450-550}$  relationships for PM<sub>10</sub>, submicron and supermicron particles are shown in Figure  
493 7a-c. The observed  $AAE$  values at both sites fall in a fairly narrow range centered around 1.2 for PM<sub>10</sub> and  
494 submicron particles, with much greater scatter for supermicron particles, consistent with Figure 4. The  
495 submicron  $SAE$  values are  $>1.8$  and the supermicron  $SAE$  values are generally  $<0.2$ , while the PM<sub>10</sub>  $SAE$   
496 values span the range 0.3 – 2. The wide range of  $SAE$  values for PM<sub>10</sub> results from time-varying  
497 contributions of supermicron and submicron particles to the total scattering.

498 Cazorla et al. (2013) previously proposed a classification scheme based on the position in the  $AAE$   
499 vs.  $SAE$  space (c.f. their Figure 1). They classified particles with  $AAE < 1$  and  $SAE > 1.5$  as “EC  
500 dominated,” and where EC stands for elemental carbon (which is approximately equivalent to BC  
501 (Andreae and Gelencser, 2006; Lack et al., 2014)). Here, almost none of the observations fall in this space,  
502 despite the submicron absorption being dominated by black carbon. Instead, the submicron measurements



503 fall primarily in the space encompassed by  $1 < AAE < 1.5$  and  $SAE > 2$ , which Cazorla et al. (2013)  
504 classified as an “EC/OC mixture” and where an implicit assumption was that the OC (organic carbon)  
505 was absorbing in nature (i.e. BrC), thus leading to the elevated  $AAE$  values compared to the “EC  
506 dominated” region. These *in situ* measurements therefore suggest that the “EC/OC mixture” region should  
507 better be classified as “EC dominated” (or equivalently “BC dominated”). These measurements indicate  
508 that BrC contributions to submicron absorption can only be clearly identified if the  $AAE$  is well-above  
509 1.5. Given that almost none of the submicron  $AAE$  values were  $< 1$ , the suggestion by Bahadur et al.  
510 (2012) that a “low-end baseline”  $AAE$  value of  $0.55 (\pm 0.24)$  that is related to “pure EC” seems unlikely  
511 to be correct and is more likely a result of a subset of the data points considered in that study having large  
512 uncertainties due to low signal levels. (Lower  $AAE$  values can be obtained if a wavelength pair is selected  
513 in which the wavelengths differ substantially and there is curvature in the  $b_{\text{abs}}$  vs. wavelength relationship  
514 (Bergstrom et al., 2007).) This conclusion is consistent with that of (Russell et al., 2010) and with the *in*  
515 *situ* observations of (Yang et al., 2009) and the remote sensing observations of (Giles et al., 2012).

516 Cazorla et al. (2013) also classified particles having  $1 < AAE < 1.5$  and  $SAE < 1$  as being a “Dust/EC  
517 mix”, and those with  $AAE < 1$  and  $SAE < 1$  as being “Coated large particles.” As the supermicron  
518 contribution to scattering increases (and the  $SAE$  decreases), the observed  $AAE$  values, at T1 especially,  
519 do not strongly deviate from the 1-1.5 range. The supermicron particles sampled here were a mixture of  
520 sea spray and dust in varying amounts. This therefore suggests that the “Dust/EC mix” regime should be  
521 reclassified to be more general, as it is not specific to “dust,” only to “large particle/BC mixtures.” The  
522 measurements suggest that dust contributions can only be clearly elucidated when the  $AAE > 1.5$ , although  
523 even when such large  $AAE$  values are observed care must be taken if the absolute absorption values are  
524 small (as is the case here for supermicron particles), corresponding to individual  $AAE$  values with  
525 substantial uncertainties. Similar caution is suggested for identification of particles in the “Coated large  
526 particle” regime, as classified by Cazorla et al. (2013). The *in situ* measurements here suggest that  
527 observations that fall within this regime are likely the result of measurement uncertainties due to low  
528 signal levels, and do not correspond to the presence of “Coated large particles.” Based on the observations  
529 here, a new classification scheme using the  $AAE$  and  $SAE$  relationship is proposed (Figure 7d).

### 530 3.1.3 Light backscattering

531 The extent to which particles scatter light in the backward versus forward direction has an important  
532 controlling influence on their climate impacts (Haywood and Shine, 1995). The backscatter fractions at  
533 550 nm for  $PM_{10}$ ,  $f_{\text{bsca},550,PM_{10}}$ , measured by the nephelometer ranged from 0.1 to 0.23, with an average  
534 value of  $0.137 \pm 0.024$  for T0 and  $0.155 \pm 0.054$  for T1. These correspond to a  $g_{\text{sca}}$  range for  $PM_{10}$  of 0.40



535 to 0.67 and mean values of  $0.57 \pm 0.056$  for T0 and  $0.53 \pm 0.054$  for T1. This range of observed values is  
536 comparable to measurements made at other locations (Andrews et al., 2006), but the averages are  
537 somewhat smaller than  $g_{\text{sca}}$  values calculated by *Kassianov et al.* (2012) at 500 nm for the T0 and T1 sites  
538 (both  $g_{\text{sca},500} = 0.65$ ). The observed  $g_{\text{sca}}$  versus  $f_{\text{sca},\text{PM}_{10}}$  relationship is shown in Figure 8b,c for T0 and T1.  
539 There is some general decrease in  $g_{\text{sca}}$  when  $f_{\text{sca},\text{PM}_{10}}$  increases at both sites, more clearly at T1 than at T0,  
540 but at both sites there is substantial scatter in the data. Some of this scatter appears to be driven by  
541 variations in the size of the submicron mode, as characterized by  $d_{\text{p,surf},\text{PM}_{10}}$ . In general, for a given  $f_{\text{sca},\text{PM}_{10}}$   
542 the observed  $g_{\text{sca}}$  values are smaller when  $d_{\text{p,surf},\text{PM}_{10}}$  is smaller.

543 This observed behavior is generally consistent with theoretical expectations. The theoretical  
544 relationship between  $g_{\text{sca}}$  and particle size for spherical particles is shown in Figure 8a. The calculated  $g_{\text{sca}}$   
545 increases nearly monotonically for diameters up to about 500 nm, reaching  $g_{\text{sca}} \sim 0.75$ . In the supermicron  
546 range above 1.5  $\mu\text{m}$  the  $g_{\text{sca}}$  is relatively constant around 0.75. In between 500 nm and 1.5  $\mu\text{m}$ , the  $g_{\text{sca}}$   
547 exhibits a more complicated dependence on size. The steepness of the  $g_{\text{sca}}$  versus  $d_{\text{p}}$  relationship between  
548 100 and 500 nm means that the observed  $g_{\text{sca}}$  for  $\text{PM}_{10}$  will be particularly sensitive to variations in the  
549 submicron particle size distribution. However, the  $g_{\text{sca}}$  will be less sensitive to variations in the  
550 supermicron particle size distribution because the  $d_{\text{p}}$  versus  $g_{\text{sca}}$  relationship is generally flatter. Further,  
551 we might expect some relationship between  $g_{\text{sca}}$  and the fraction of scattering due to sub- or supermicron  
552 particles to the extent that the two size regimes have generally distinct  $g_{\text{sca}}$  values. Indeed, such behavior  
553 is seen in the observations, in large part because the  $d_{\text{p,surf},\text{PM}_{10}}$  values vary within the sensitive range (100-  
554 500 nm).

555 Therefore, in an effort to account for this apparent co-dependence of  $g_{\text{sca}}$  on  $f_{\text{sca},\text{PM}_{10}}$  and  $d_{\text{p,surf},\text{PM}_{10}}$ ,  
556 the  $f_{\text{sca},\text{PM}_{10}}$  values have been divided by the  $d_{\text{p,surf},\text{PM}_{10}}$  values, with the ratio indicated as  $R_{\text{g}}$ . There is, in  
557 general, a much stronger relationship between the  $g_{\text{sca}}$  values and  $R_{\text{g}}$  (Figure 8d,e) than there is with  $f_{\text{sca},\text{PM}_{10}}$   
558 alone, and much of the residual scatter seems to be driven by variations in the supermicron size  
559 distribution. Linear fits give  $g_{\text{sca}} = -38.5R_{\text{g}} + 0.66$  for T0 ( $r^2 = 0.51$ ) and  $g_{\text{sca}} = -51.5R_{\text{g}} + 0.66$  for T1 ( $r^2 =$   
560  $0.71$ ), and where  $d_{\text{p,surf},\text{PM}_{10}}$  is in nm. Overall, the observations here demonstrate that the observable  
561 backscatter coefficients depend importantly on the relative contributions of sub- versus supermicron  
562 particles to the total scattering, but that the specific relationship between backscatter and the sub- or  
563 supermicron scattering fraction is obscured by variations in the size distribution within each size range.  
564 However, the greatest sensitivity of  $g_{\text{sca}}$  is found for size variations within the submicron size range.



### 565 **3.2 Influence of heating on optical properties**

566 At the T0 site, the UCD CRD and PAS instruments sampled alternately dried, ambient particles  
567 (PM<sub>2.5</sub>) or particles that had been passed through a thermodenuder (TD) that was held at 225 °C during  
568 the study. As particles pass through the TD, some materials evaporate, including ammonium nitrate,  
569 ammonium sulfate and many organics, while others do not, including black carbon, dust and sea salt. Loss  
570 of these materials leads to changes in the optical properties, including the particle optically-weighted  
571 hygroscopicity. The influence of heating on the optical properties is used here to further probe the particle  
572 composition.

573 The observed fraction of extinction remaining after heating,  $f_{\text{ext},\text{TD}}$ , for PM<sub>2.5</sub> varied from ~0.15 to  
574 0.6, suggesting a wide range of particle volatility. This variability is strongly linked to the relative  
575 contribution of sub- versus supermicron particles to the observed extinction; an approximately linear  
576 relationship (with a positive slope) between  $f_{\text{ext},\text{TD}}$  and the *EAE* measured for the ambient particles was  
577 observed (Figure 9). This increase in  $f_{\text{ext},\text{TD}}$  with decreasing *EAE* suggests that the supermicron  
578 components are mostly non-volatile, consistent with a likely dust or sea salt contribution as identified  
579 above. Further, this suggests that  $f_{\text{ext},\text{TD}}$  can be used as an indicator of particle size in the current study.  
580 There is a cluster of points at the highest  $f_{\text{ext},\text{TD}}$  (the light green points in Figure 9) that were observed  
581 during a specific overnight period when we suspect that the site was briefly impacted by large particles  
582 produced as part of local road resurfacing.

583 The bulk particle hygroscopicity, characterized by  $\gamma_{\text{RH}}$ , did not vary monotonically with  $f_{\text{ext},\text{TD}}$   
584 (Figure 10a). This is because the observed hygroscopicity depends on compositional variability within  
585 both the sub- and supermicron modes (Atkinson et al., 2015). However, the change in the hygroscopicity  
586 upon heating,  $\Delta\gamma_{\text{RH}} = \gamma_{\text{RH,ambient}} - \gamma_{\text{RH,TD}}$ , does exhibit a clear correlation with  $f_{\text{ext},\text{TD}}$ , with larger  $\Delta\gamma_{\text{RH}}$   
587 corresponding to smaller  $f_{\text{ext},\text{TD}}$ , i.e. for smaller, typically more volatile particles (Figure 10b). The  
588 observed  $\Delta\gamma_{\text{RH}}$  appear to cross over zero around  $f_{\text{ext},\text{TD}} = 0.4$ . Apparently, for smaller particles that exhibit  
589 greater overall mass loss upon heating, the  $\gamma_{\text{RH}}$  tends to decrease with heating. This is as might be  
590 expected, since one key residual component will be non-hygroscopic BC when the distribution is  
591 dominated by smaller particles. However, when the distribution is dominated by larger particles,  
592 evaporation leads to the residual particles appearing, on average, slightly more hygroscopic. This suggests  
593 that the supermicron components that are susceptible to evaporation are lower-hygroscopicity material,  
594 most likely organics but also, potentially, inorganics such as sulfate and nitrate, which have lower  
595 hygroscopicity than sodium chloride. Some of the sea salt-containing particles observed during CARES  
596 were found to be internally mixed with organics (likely organic acids) that displaced chloride (Laskin et



597 al., 2012), and organic salts are generally less hygroscopic than sea salt (Drozd et al., 2014). It is possible  
598 that these organics evaporated in the TD, leaving behind more hygroscopic material, although such a  
599 hypothesis requires further investigation.

600 The contribution to the total light absorption from non-BC materials that evaporate in the TD was  
601 characterized by the absorption enhancement,  $E_{\text{abs}}$ , which is here taken as the ratio between the ambient  
602 and thermodenuded  $b_{\text{abs}}$ . We have previously investigated the dependence of  $E_{\text{abs}}$  on photochemical age  
603 at CARES using the same data set as is being considered here, and separately the dependence on the  
604 relative amount of “coating” (non-BC) material that is internally mixed with BC at the CalNex field study  
605 (Cappa et al., 2012). It was found that the  $E_{\text{abs}}$  increases by only a small amount as PCA and coating  
606 amount increased. Here, we see that  $E_{\text{abs}}$  exhibits some slight dependence on  $f_{\text{ext,TD}}$ , with somewhat larger  
607 values observed at smaller  $f_{\text{ext,TD}}$  (Figure 10c,d). It is difficult to establish whether this dependence  
608 indicates that larger  $E_{\text{abs}}$  would have been observed in Cappa et al. (2012) for the CARES dataset had  
609 more material evaporated, but given that the  $f_{\text{ext,TD}}$  here is determined predominately by changes in the  
610 relative contributions from sub- and supermicron particles this seems unlikely. (The complementary  
611 measurements from CalNex were for  $\text{PM}_{10}$ , not  $\text{PM}_{2.5}$  as here, and thus the influence of supermicron  
612 particles on the observations was substantially smaller during that study. For reference, the CalNex  
613 campaign-average submicron  $SAE$  for the 450-550 nm pair was 2.1. Thus, the conclusions here for the  
614 CARES dataset are not necessarily applicable to the interpretation of the CalNex dataset.) Further, a fit  
615 of the mean binned values of  $E_{\text{abs}}$  extrapolated to  $f_{\text{ext,TD}} = 0$  gives only  $E_{\text{abs}} = 1.14 (\pm 0.02)$  and  $1.29 (\pm 0.06)$   
616 at 532 nm and 405 nm, respectively, suggesting that substantially larger values than the observed range  
617 would not have been likely had a greater extent of evaporation been observed. The larger extrapolated  
618 value at 405 nm than at 532 nm is consistent with a small contribution from so-called “brown carbon,”  
619 which has an absorption spectrum that strongly increases towards shorter wavelengths, to the observed  
620 absorption.

621 The particle single scatter albedo exhibits a non-monotonic dependence on  $f_{\text{ext,TD}}$  at both 532 nm  
622 and 405 nm (Figure 10e,f). On average, the ambient SSA values are at a minimum of 0.85 around  $f_{\text{ext,TD}}$   
623 = 0.35. The SSA then increases at either larger or smaller  $f_{\text{ext,TD}}$ . The increase in SSA towards smaller  
624  $f_{\text{ext,TD}}$  likely reflects an increasing contribution of secondary aerosol species within the submicron mode  
625 (e.g. organics, ammonium sulfate, ammonium nitrate) relative to BC, leading the overall particulates to  
626 appear both more volatile and more scattering. Indeed, HR-AMS measurements indicate that secondary  
627 inorganic and organic species are dominant components of the submicron particles in the Sacramento and  
628 Sierra Nevada foothill region during CARES (Setyan et al., 2012; Shilling et al., 2013). The increase in



629 SSA towards larger  $f_{\text{ext,TD}}$  likely results from the increasing contribution of non-volatile sea salt and dust  
630 components within the supermicron mode that are either non- or very weakly absorbing. Looking at the  
631 change in SSA upon heating in the TD,  $\Delta\text{SSA}$ , there is a clear increase in  $\Delta\text{SSA}$  with decreasing  $f_{\text{ext,TD}}$   
632 (Figure 10g,h). This is as expected because if material does not evaporate then no change in SSA should  
633 be observed. The  $\Delta\text{SSA}$  linearly extrapolated to  $f_{\text{ext,TD}} = 0$  is 0.46 ( $\pm 0.02$ ) and 0.50 ( $\pm 0.02$ ) at 532 nm and  
634 405 nm, respectively, corresponding to absolute extrapolated SSA values of  $\sim 0.4$  given the observed  
635 ambient particle SSA values. (Linear extrapolation to zero is not fully justifiable because the  $f_{\text{ext,TD}}$  cannot  
636 go to zero if there is some BC around and because there appears to be some flattening off in the  $\Delta\text{SSA}$   
637 values at smaller  $f_{\text{ext,TD}}$ . Nonetheless, it can provide an estimate in the limit of small BC contributions.)  
638 These extrapolated SSA values are relatively large compared to some laboratory observations for “fresh”  
639 BC particles that are produced, for example, from flames (Cross et al., 2010) or gasoline or diesel vehicles  
640 (Schneider et al., 2005; Forestieri et al., 2013) and that have little intrinsic organic material, but slightly  
641 smaller than that reported by one other laboratory study on flame-generated soot (Radney et al., 2014).  
642 Primary emitted BC has a fractal-like structure that is thought to collapse over time through atmospheric  
643 ageing processes. This change in shape due to collapse is thought to lead to an increase in the SSA,  
644 separate from any contributions from scattering coating materials (Chakrabarty et al., 2014). That the  
645 extrapolated SSA values are larger than many of the laboratory studies on fresh BC suggests that the  
646 sampled particles were somewhat collapsed compared to their emitted state.

647 For the period where the T0 site was impacted by particles emitted from local road surfacing  
648 activities (e.g. asphalt), the ambient SSA values are small and the  $\Delta\text{SSA}$  values deviate from the general  
649 relationship observed for other periods. In fact, the absolute SSA measured for thermodenuded particles  
650 during this particular period are around zero at 405 nm but  $\sim 0.2$  at 532 nm. Such very small SSA values  
651 suggest that absorption is dominated by very small particles, or at least particles that are agglomerates of  
652 very small spherules; the surface area-weighted size distribution measured during this period peaked  
653 around 300 nm diameter and the SP2 BC particle size distributions clearly indicate that the overall BC  
654 particle size was larger during the asphalt-impacted period (Figure S9), suggesting that agglomerates of  
655 small spherules is most plausible. We cannot entirely rule out the possibility that the measurements during  
656 this period were strongly impacted by some absorbing gas-phase species (e.g.  $\text{NO}_2$ ), confounding the SSA  
657 measurements, although there was no evidence of gas-phase absorption in the background CRD channels  
658 during this period suggesting that this is unlikely.



#### 659 **4 Conclusions**

660 Optical property measurements of  $PM_{10}$ ,  $PM_{2.5}$  and  $PM_{10}$  made during the CARES 2010 field study  
661 have been examined to develop understanding of the relationships between various intensive properties  
662 and to establish differences in behavior between sub- and supermicron PM. Measurements were made at  
663 two sites in the Sacramento region, one urban (T0) and one more rural (T1) but impacted by the urban  
664 outflow on most days under southwesterly flow conditions (Fast et al., 2012). At both sites, there is a  
665 strong contribution of supermicron particles to the total scattering, averaging around 50% at both sites.  
666 The source of these supermicron particles appears to be a combination of local dust and sea spray, along  
667 with some contributions from penetration of traditionally submicron particles into the supermicron mode.  
668 The specific contributions of any of these supermicron particle sources varies with time and depends on  
669 the prevailing transport patterns with, perhaps not surprisingly, generally larger sea spray contributions  
670 when air masses have been transported from the San Francisco Bay Area. The measured scattering  
671 Ångstrom exponents (*SAE*) for  $PM_{10}$  are strongly correlated with the submicron versus supermicron  
672 fraction of the total scattering, with similar linear relationships observed at both sites. This relationship  
673 held despite there being variations in the size distributions within a given mode, which can theoretically  
674 alter the *SAE*. This suggests that the relationships determined here are quite general, and that the *SAE* can  
675 be used to quantitatively attribute scattering to sub- and supermicron particles. There was no notable  
676 dependence of the absorption Ångstrom exponent (*AAE*) on *SAE* for  $PM_{10}$ , and these observations were  
677 used to propose an updated particle classification scheme based on the relationship between these two  
678 parameters.

679 The influence of photochemical processing on the sub- versus supermicron contribution to scattering  
680 differed between the two sites, with photochemical processing leading to an increase in the submicron  
681 fraction of scattering for the T0 (urban) site but minimal change, or even a slight decrease, at the T1  
682 (downwind) site. This reflects in part the strong daytime peak in photochemical age at the T0 site in  
683 contrast to the more gradual increase at the T1 site, coupled with the much stronger diurnal profile in the  
684 wind speed, with a daytime peak, at the T1 site. Consequently, at the T1 site, photochemical production  
685 of secondary PM was spread over a wider range of times due to transport and was countered through  
686 local, temporally similar increases in dust production due to the higher daytime winds. At the T0 site, the  
687 strong photochemical production of secondary PM led to a clear increase in the submicron fraction of  
688 scattering with photochemical ageing.

689 The mass scattering coefficient for the supermicron particles varied inversely with the median  
690 surface-weighted particle diameter ( $d_{p,surf}$ ) of the supermicron mode, in general accordance with



691 theoretical expectations. This indicates clear temporal variability in the nature of the supermicron particle  
692 sources, which seem to be coupled to the prevailing wind direction or air mass history, as established  
693 through consideration of back trajectories. Light absorption was dominated by submicron particles,  
694 although there was some contribution from the supermicron particles. The mass absorption coefficient for  
695 supermicron particles exhibited a clear dependence on the supermicron  $d_{p,surf}$ , most likely due to variations  
696 in the relative contributions of non-absorbing sea spray particles, penetration of BC from the submicron  
697 mode, and very weak absorption by supermicron dust particles. Particle backscatter was found to be  
698 related to the relative fractions of sub- versus supermicron scattering, but with an additional sensitivity to  
699 variations in the size distribution within the submicron size range. The susceptibility of the particles to  
700 heating in a thermodenuder depended explicitly on the contribution of supermicron particles to the  $PM_{2.5}$   
701 extinction, most likely because a large fraction of the supermicron particles were either essentially non-  
702 volatile sea spray or dust particles. Heating in general led to an increase in the average particle  
703 hygroscopicity and a decrease in the single scatter albedo. These together indicate that the residual  
704 particles are likely a combination of absorbing submicron BC and somewhat hygroscopic supermicron  
705 sea spray and less hygroscopic dust. The results presented here demonstrate that optical property  
706 measurements can be used to assess likely chemical differences in the contributing particle types, and thus  
707 to identify key PM sources.

## 708 **Author Information**

709 Corresponding Author: Christopher D. Cappa

710 E-mail: [cdcappa@ucdavis.edu](mailto:cdcappa@ucdavis.edu)

711 The authors declare no competing financial interest.

## 712 **Acknowledgements**

713 This work was supported by the Atmospheric System Research (ASR) program sponsored by the  
714 US Department of Energy (DOE), Office of Biological and Environmental Research (OBER), including  
715 Grant No. DE-SC0008937. The authors acknowledge W. Berk Knighton for the PTR-MS data at the T1  
716 site, R. Subramanian for the SP2 data, Ari Setyan for collection of the SMPS data at the T1 site and B.  
717 Tom Jobson for the  $NO_x$ ,  $NO_y$ , PTR-MS and meteorological data at the T0 site. The authors acknowledge  
718 the NOAA Air Resources Laboratory (ARL) for the provision of the HYSPLIT transport and dispersion  
719 model (<http://www.ready.noaa.gov>) used in this publication. The backscattering Mie calculations were  
720 performed using MiePlot from Philip Laven ([www.philiplaven.com/mieplot.htm](http://www.philiplaven.com/mieplot.htm)). Funding for data



721 collection was provided by the US DOE's Atmospheric Radiation Measurement (ARM) Program. All  
722 data used in this study are available from the ARM data archive at:  
723 <http://www.arm.gov/campaigns/aaf2009carbonaerosol>. The views expressed in this document are solely  
724 those of the authors and the funding agencies do not endorse any products or commercial services  
725 mentioned in this publication.

## 726 References

727 Anderson, T. L., Masonis, S. J., Covert, D. S., Ahlquist, N. C., Howell, S. G., Clarke, A. D., and  
728 McNaughton, C. S.: Variability of aerosol optical properties derived from in situ aircraft measurements  
729 during ACE-Asia, *J. Geophys. Res.*, 108, 8647, doi:10.1029/2002JD003247, 2003.

730 Anderson, T. L. and Ogren, J. A.: Determining Aerosol Radiative Properties Using the TSI 3563  
731 Integrating Nephelometer, *Aerosol Sci. Technol.*, 29, 57-69, doi:10.1080/02786829808965551, 1998.

732 Andreae, M. O. and Gelencser, A.: Black carbon or brown carbon? The nature of light-absorbing  
733 carbonaceous aerosols, *Atmos. Chem. Phys.*, 6, 3131-3148, 2006.

734 Andrews, E., Sheridan, P. J., Fiebig, M., McComiskey, A., Ogren, J. A., Arnott, P., Covert, D.,  
735 Elleman, R., Gasparini, R., Collins, D., Jonsson, H., Schmid, B., and Wang, J.: Comparison of methods  
736 for deriving aerosol asymmetry parameter, *J. Geophys. Res.-Atmos.*, 111, D05S04,  
737 doi:10.1029/2004JD005734, 2006.

738 Atkinson, D. B., Radney, J. G., Lum, J., Kolesar, K. R., Cziczo, D. J., Pekour, M. S., Zhang, Q.,  
739 Setyan, A., Zelenyuk, A., and Cappa, C. D.: Aerosol optical hygroscopicity measurements during the  
740 2010 CARES campaign, *Atmos. Chem. Phys.*, 15, 4045-4061, doi:10.5194/acp-15-4045-2015, 2015.

741 Atkinson, R., Baulch, D. L., Cox, R. A., Crowley, J. N., Hampson, R. F., Hynes, R. G., Jenkin,  
742 M. E., Rossi, M. J., Troe, J., and Subcommittee, I.: Evaluated kinetic and photochemical data for  
743 atmospheric chemistry: Volume II - gas phase reactions of organic species, *Atmos. Chem. Phys.*, 6,  
744 3625-4055, doi:10.5194/acp-6-3625-2006, 2006.

745 Bahadur, R., Praveen, P. S., Xu, Y., and Ramanathan, V.: Solar absorption by elemental and  
746 brown carbon determined from spectral observations, *Proc. Nat. Acad. Sci.*, 109, 17366-17371,  
747 doi:10.1073/pnas.1205910109, 2012.

748 Bates, T. S., Anderson, T. L., Baynard, T., Bond, T., Boucher, O., Carmichael, G., Clarke, A.,  
749 Erlick, C., Guo, H., Horowitz, L., Howell, S., Kulkarni, S., Maring, H., McComiskey, A., Middlebrook,  
750 A., Noone, K., O'Dowd, C. D., Ogren, J., Penner, J., Quinn, P. K., Ravishankara, A. R., Savoie, D. L.,  
751 Schwartz, S. E., Shinozuka, Y., Tang, Y., Weber, R. J., and Wu, Y.: Aerosol direct radiative effects over



- 752 the northwest Atlantic, northwest Pacific, and North Indian Oceans: estimates based on in-situ chemical  
753 and optical measurements and chemical transport modeling, *Atmos. Chem. Phys.*, 6, 1657-1732, 2006.
- 754 Bergstrom, R. W., Pilewskie, P., Russell, P. B., Redemann, J., Bond, T. C., Quinn, P. K., and  
755 Sierau, B.: Spectral absorption properties of atmospheric aerosols, *Atmos. Chem. Phys.*, 7, 5937-5943,  
756 doi:10.5194/acp-7-5937-2007, 2007.
- 757 Bohren, C. F. and Huffman, D. R.: Absorption and scattering of light by small particles, Wiley,  
758 New York, 1983.
- 759 Bond, T. C., Anderson, T. L., and Campbell, D.: Calibration and intercomparison of filter-based  
760 measurements of visible light absorption by aerosols, *Aerosol Sci. Technol.*, 30, 582-600,  
761 doi:10.1080/027868299304435, 1999.
- 762 Brown, S. S., Talukdar, R. K., and Ravishankara, A. R.: Rate constants for the reaction  
763  $\text{OH} + \text{NO}_2 + \text{M} \rightarrow \text{HNO}_3 + \text{M}$  under atmospheric conditions, *Chem. Phys. Lett.*, 299, 277-284,  
764 doi:10.1016/S0009-2614(98)01283-4, 1999.
- 765 California Air Resources Board: Characterization of ambient PM10 and PM2.5 in California.  
766 Sacramento, CA, 2005; <http://www.arb.ca.gov/pm/pmmeasures/pmch05/pmch05.htm>.
- 767 Canagaratna, M. R., Jayne, J. T., Jimenez, J. L., Allan, J. D., Alfarra, M. R., Zhang, Q., Onasch,  
768 T. B., Drewnick, F., Coe, H., Middlebrook, A., Delia, A., Williams, L. R., Trimborn, A. M., Northway,  
769 M. J., DeCarlo, P. F., Kolb, C. E., Davidovits, P., and Worsnop, D. R.: Chemical and microphysical  
770 characterization of ambient aerosols with the Aerodyne aerosol mass spectrometer, *Mass Spectrom.*  
771 *Rev.*, 26, 185-222, doi:10.1002/mas.20115, 2007.
- 772 Cappa, C. D., Onasch, T. B., Massoli, P., Worsnop, D., Bates, T. S., Cross, E., Davidovits, P.,  
773 Hakala, J., Hayden, K., Jobson, B. T., Kolesar, K. R., Lack, D. A., Lerner, B., Li, S. M., Mellon, D.,  
774 Nuaanman, I., Olfert, J., Petaja, T., Quinn, P. K., Song, C., Subramanian, R., Williams, E. J., and  
775 Zaveri, R. A.: Radiative absorption enhancements due to the mixing state of atmospheric black carbon  
776 *Science*, 337, 1078-1081, doi:10.1126/science.1223447, 2012.
- 777 Cappa, C. D., Williams, E. J., Lack, D. A., Buffaloe, G. M., Coffman, D., Hayden, K. L.,  
778 Herndon, S. C., Lerner, B. M., Li, S. M., Massoli, P., McLaren, R., Nuaaman, I., Onasch, T. B., and  
779 Quinn, P. K.: A case study into the measurement of ship emissions from plume intercepts of the NOAA  
780 Ship Miller Freeman, *Atmos. Chem. Phys.*, 14, 1337-1352, doi:doi:10.5194/acp-14-1337-2014, 2014.
- 781 Cazorla, A., Bahadur, R., Suski, K. J., Cahill, J. F., Chand, D., Schmid, B., Ramanathan, V., and  
782 Prather, K. A.: Relating aerosol absorption due to soot, organic carbon, and dust to emission sources  
783 determined from in-situ chemical measurements, *Atmos. Chem. Phys.*, 13, 9337-9350, doi:10.5194/acp-  
784 13-9337-2013, 2013.



- 785 Chakrabarty, R. K., Beres, N. D., Moosmuller, H., China, S., Mazzoleni, C., Dubey, M. K., Liu,  
786 L., and Mishchenko, M. I.: Soot superaggregates from flaming wildfires and their direct radiative  
787 forcing, *Scientific Reports*, 4, 5508, doi:10.1038/srep05508, 2014.
- 788 Chung, C. E., Ramanathan, V., and Decremmer, D.: Observationally constrained estimates of  
789 carbonaceous aerosol radiative forcing, *Proc. Nat. Acad. Sci.*, 109, 11624-11629,  
790 doi:10.1073/pnas.1203707109, 2012.
- 791 Clarke, A., Shinozuka, Y., Kapustin, V. N., Howell, S., Huebert, B. J., Doherty, S. J., Anderson,  
792 T. L., Covert, D., Anderson, J., Hua, X., Moore II, K. G., McNaughton, C., Carmichael, G., and Weber,  
793 R.: Size distributions and mixtures of dust and black carbon aerosol in Asian outflow: Physiochemistry  
794 and optical properties, *J. Geophys. Res.*, 109, D15S09, doi:10.1029/2003JD004378, 2004.
- 795 Costabile, F., Barnaba, F., Angelini, F., and Gobbi, G. P.: Identification of key aerosol  
796 populations through their size and composition resolved spectral scattering and absorption, *Atmos.*  
797 *Chem. Phys.*, 13, 2455-2470, doi:10.5194/acp-13-2455-2013, 2013.
- 798 Cross, E. S., Onasch, T. B., Ahern, A., Wrobel, W., Slowik, J. G., Olfert, J., Lack, D. A.,  
799 Massoli, P., Cappa, C. D., Schwarz, J. P., Spackman, J. R., Fahey, D. W., Sedlacek, A., Trimborn, A.,  
800 Jayne, J. T., Freedman, A., Williams, L. R., Ng, N. L., Mazzoleni, C., Dubey, M., Brem, B., Kok, G.,  
801 Subramanian, R., Freitag, S., Clarke, A., Thornhill, D., Marr, L. C., Kolb, C. E., Worsnop, D. R., and  
802 Davidovits, P.: Soot Particle Studies—Instrument Inter-Comparison—Project Overview, *Aerosol Sci.*  
803 *Technol.*, 44, 592 - 611, doi:10.1080/02786826.2010.482113, 2010.
- 804 Cziczo, D. J., Thomson, D. S., Thompson, T. L., DeMott, P. J., and Murphy, D. M.: Particle  
805 analysis by laser mass spectrometry (PALMS) studies of ice nuclei and other low number density  
806 particles, *Int. J. Mass Spectrom.*, 258, 21-29, doi:10.1016/j.ijms.2006.05.013, 2006.
- 807 Draxler, R. R. and Rolph, G. D.: HYSPLIT (HYbrid Single-Particle Lagrangian Integrated  
808 Trajectory) Model access via NOAA ARL READY Website, <http://www.arl.noaa.gov/HYSPLIT.php>,  
809 NOAA Air Resources Laboratory, College Park, MD, USA, last access: 29 August 2015, 2015.
- 810 Drozd, G., Woo, J., Hakkinen, S. A. K., Nenes, A., and McNeill, V. F.: Inorganic salts interact  
811 with oxalic acid in submicron particles to form material with low hygroscopicity and volatility, *Atmos.*  
812 *Chem. Phys.*, 14, 5205-5215, doi:10.5194/acp-14-5205-2014, 2014.
- 813 Ewing, S. A., Christensen, J. N., Brown, S. T., Vancuren, R. A., Cliff, S. S., and Depaolo, D. J.:  
814 Pb Isotopes as an Indicator of the Asian Contribution to Particulate Air Pollution in Urban California,  
815 *Environ. Sci. Technol.*, 44, 8911-8916, doi:10.1021/es101450t, 2010.
- 816 Fast, J. D., Gustafson Jr, W. I., Berg, L. K., Shaw, W. J., Pekour, M., Shrivastava, M., Barnard,  
817 J. C., Ferrare, R. A., Hostetler, C. A., Hair, J. A., Erickson, M., Jobson, B. T., Flowers, B., Dubey, M.



- 818 K., Springston, S., Pierce, R. B., Dolislager, L., Pederson, J., and Zaveri, R. A.: Transport and mixing  
819 patterns over Central California during the carbonaceous aerosol and radiative effects study (CARES),  
820 Atmos. Chem. Phys., 12, 1759-1783, doi:10.5194/acp-12-1759-2012, 2012.
- 821 Forestieri, S. D., Collier, S., Kuwayama, T., Zhang, Q., Kleeman, M. J., and Cappa, C. D.: Real-  
822 Time Black Carbon Emission Factor Measurements from Light Duty Vehicles, Environ. Sci. Technol.,  
823 47, 13104-13112, doi:10.1021/es401415a, 2013.
- 824 Garland, R. M., Yang, H., Schmid, O., Rose, D., Nowak, A., Achtert, P., Wiedensohler, A.,  
825 Takegawa, N., Kita, K., Miyazaki, Y., Kondo, Y., Hu, M., Shao, M., Zeng, L. M., Zhang, Y. H.,  
826 Andreae, M. O., and Pöschl, U.: Aerosol optical properties in a rural environment near the mega-city  
827 Guangzhou, China: implications for regional air pollution, radiative forcing and remote sensing, Atmos.  
828 Chem. Phys., 8, 5161-5186, doi:10.5194/acp-8-5161-2008, 2008.
- 829 Giles, D. M., Holben, B. N., Eck, T. F., Sinyuk, A., Smirnov, A., Slutsker, I., Dickerson, R. R.,  
830 Thompson, A. M., and Schafer, J. S.: An analysis of AERONET aerosol absorption properties and  
831 classifications representative of aerosol source regions, 117, D17203, doi:10.1029/2012JD018127,  
832 2012.
- 833 Ginoux, P., Prospero, J. M., Gill, T. E., Hsu, N. C., and Zhao, M.: Global-scale attribution of  
834 anthropogenic and natural dust sources and their emission rates based on MODIS Deep Blue aerosol  
835 products, Rev. Geophys., 50, RG3005, doi:10.1029/2012RG000388, 2012.
- 836 Gyawali, M., Arnott, W. P., Lewis, K., and Moosmüller, H.: In situ aerosol optics in Reno, NV,  
837 USA during and after the summer 2008 California wildfires and the influence of absorbing and non-  
838 absorbing organic coatings on spectral light absorption, Atmos. Chem. Phys., 9, 8007-8015,  
839 doi:10.5194/acp-9-8007-2009, 2009.
- 840 Gysel, M., Laborde, M., Olfert, J. S., Subramanian, R., and Gröhn, A. J.: Effective density of  
841 Aquadag and fullerene soot black carbon reference materials used for SP2 calibration, Atmos. Meas.  
842 Technol., 4, 2851-2858, doi:10.5194/amt-4-2851-2011, 2011.
- 843 Haywood, J. M. and Shine, K. P.: The Effect of Anthropogenic Sulfate and Soot Aerosol on the  
844 Clear-Sky Planetary Radiation Budget, Geophys. Res. Lett., 22, 603-606, doi:10.1029/95GL00075,  
845 1995.
- 846 Huffman, J. A., Ziemann, P. J., Jayne, J. T., Worsnop, D. R., and Jimenez, J. L.: Development  
847 and characterization of a fast-stepping/scanning thermodenuder for chemically-resolved aerosol  
848 volatility measurements, Aerosol Sci. Technol., 42, 395-407, doi:10.1080/02786820802104981, 2008.



- 849 IPCC: Climate Change 2013: The Physical Science Basis. Contribution of Working Group I to  
850 the Fifth Assessment Report of the Intergovernmental Panel on Climate Change, Cambridge University  
851 Press, Cambridge, United Kingdom and New York, NY, USA, 2013.
- 852 Jung, J., Lee, H., Kim, Y. J., Liu, X., Zhang, Y., Hu, M., and Sugimoto, N.: Optical properties of  
853 atmospheric aerosols obtained by in situ and remote measurements during 2006 Campaign of Air  
854 Quality Research in Beijing (CAREBeijing-2006), *J. Geophys. Res.*, 114, n/a-n/a,  
855 doi:10.1029/2008JD010337, 2009.
- 856 Kassianov, E., Pekour, M., and Barnard, J.: Aerosols in central California: Unexpectedly large  
857 contribution of coarse mode to aerosol radiative forcing, *Geophys. Res. Lett.*, 39, L20806,  
858 doi:10.1029/2012GL053469, 2012.
- 859 Kaufman, Y. J., Tanre, D., and Boucher, O.: A satellite view of aerosols in the climate system,  
860 *Nature*, 419, 215-223, doi:10.1038/nature01091, 2002.
- 861 Laborde, M., Mertes, P., Zieger, P., Dommen, J., Baltensperger, U., and Gysel, M.: Sensitivity  
862 of the Single Particle Soot Photometer to different black carbon types, *Atmos. Meas. Tech.*, 5, 1031-  
863 1043, doi:10.5194/amt-5-1031-2012, 2012a.
- 864 Laborde, M., Schnaiter, M., Linke, C., Saathoff, H., Naumann, K. H., Möhler, O., Berlenz, S.,  
865 Wagner, U., Taylor, J. W., Liu, D., Flynn, M., Allan, J. D., Coe, H., Heimerl, K., Dahlkötter, F.,  
866 Weinzierl, B., Wollny, A. G., Zanatta, M., Cozic, J., Laj, P., Hitztenberger, R., Schwarz, J. P., and Gysel,  
867 M.: Single Particle Soot Photometer intercomparison at the AIDA chamber, *Atmos. Meas. Tech.*, 5,  
868 3077-3097, doi:10.5194/amt-5-3077-2012, 2012b.
- 869 Lack, D., Moosmüller, H., McMeeking, G., Chakrabarty, R., and Baumgardner, D.:  
870 Characterizing elemental, equivalent black, and refractory black carbon aerosol particles: a review of  
871 techniques, their limitations and uncertainties, *Anal Bioanal Chem*, 406, 99-122, doi:10.1007/s00216-  
872 013-7402-3, 2014.
- 873 Lack, D. A. and Langridge, J. M.: On the attribution of black and brown carbon light absorption  
874 using the Angstrom exponent, *Atmos. Chem. Phys.*, 13, 10535-10543, doi:10.5194/acp-13-10535-2013,  
875 2013.
- 876 Lack, D. A., Richardson, M. S., Law, D., Langridge, J. M., Cappa, C. D., McLaughlin, R. J., and  
877 Murphy, D. M.: Aircraft Instrument for Comprehensive Characterization of Aerosol Optical Properties,  
878 Part 2: Black and Brown Carbon Absorption and Absorption Enhancement Measured with Photo  
879 Acoustic Spectroscopy, *Aerosol Sci. Technol.*, 46, 555-568, doi:10.1080/02786826.2011.645955, 2012.
- 880 Langridge, J. M., Richardson, M. S., Lack, D., Law, D., and Murphy, D. M.: Aircraft Instrument  
881 for Comprehensive Characterization of Aerosol Optical Properties, Part I: Wavelength-Dependent



- 882 Optical Extinction and Its Relative Humidity Dependence Measured Using Cavity Ringdown  
883 Spectroscopy, *Aerosol Sci. Technol.*, 45, 1305-1318, doi:10.1080/02786826.2011.592745, 2011.
- 884 Laskin, A., Moffet, R. C., Gilles, M. K., Fast, J. D., Zaveri, R. A., Wang, B. B., Nigge, P., and  
885 Shutthanandan, J.: Tropospheric chemistry of internally mixed sea salt and organic particles: Surprising  
886 reactivity of NaCl with weak organic acids, *J. Geophys. Res.-Atmos.*, 117, D15302,  
887 doi:10.1029/2012jd017743, 2012.
- 888 Myhre, G., Samset, B. H., Schulz, M., Balkanski, Y., Bauer, S., Berntsen, T. K., Bian, H.,  
889 Bellouin, N., Chin, M., Diehl, T., Easter, R. C., Feichter, J., Ghan, S. J., Hauglustaine, D., Iversen, T.,  
890 Kinne, S., Kirkevåg, A., Lamarque, J. F., Lin, G., Liu, X., Luo, G., Ma, X., Penner, J. E., Rasch, P. J.,  
891 Seland, Ø., Skeie, R. B., Stier, P., Takemura, T., Tsigaridis, K., Wang, Z., Xu, L., Yu, H., Yu, F., Yoon,  
892 J. H., Zhang, K., Zhang, H., and Zhou, C.: Radiative forcing of the direct aerosol effect from AeroCom  
893 Phase II simulations, *Atmos. Chem. Phys.*, 13, 1853-1877, doi:10.5194/acp-13-1853-2013, 2012.
- 894 Nakayama, T., Kondo, Y., Moteki, N., Sahu, L. K., Kinase, T., Kita, K., and Matsumi, Y.: Size-  
895 dependent correction factors for absorption measurements using filter-based photometers: PSAP and  
896 COSMOS, *J. Aerosol Sci.*, 41, 333-343, doi:10.1016/j.jaerosci.2010.01.004, 2010.
- 897 Ogren, J. A.: Comment on “Calibration and Intercomparison of Filter-Based Measurements of  
898 Visible Light Absorption by Aerosols”, *Aerosol Sci. Technol.*, 44, 589-591,  
899 doi:10.1080/02786826.2010.482111, 2010.
- 900 Parrish, D. D., Stohl, A., Forster, C., Atlas, E. L., Blake, D. R., Goldan, P. D., Kuster, W. C., and  
901 de Gouw, J. A.: Effects of mixing on evolution of hydrocarbon ratios in the troposphere, *J. Geophys.*  
902 *Res.-Atmos.*, 112, D10S34, doi:10.1029/2006JD007583, 2007.
- 903 Quinn, P. K., Coffman, D. J., Bates, T. S., Welton, E. J., Covert, D. S., Miller, T. L., Johnson, J.  
904 E., Maria, S., Russell, L., Arimoto, R., Carrico, C. M., Rood, M. J., and Anderson, J.: Aerosol optical  
905 properties measured on board the Ronald H. Brown during ACE-Asia as a function of aerosol chemical  
906 composition and source region, *J. Geophys. Res.-Atmos.*, 109, doi:D19s01  
907 Artn d19s01, 2004.
- 908 Radney, J. G., You, R., Ma, X., Conny, J. M., Zachariah, M. R., Hodges, J. T., and Zangmeister,  
909 C. D.: Dependence of Soot Optical Properties on Particle Morphology: Measurements and Model  
910 Comparisons, *Environ. Sci. Technol.*, 48, 3169-3176, doi:10.1021/es4041804, 2014.
- 911 Roberts, J. M., Fehsenfeld, F. C., Liu, S. C., Bollinger, M. J., Hahn, C., Albritton, D. L., and  
912 Sievers, R. E.: Measurements of aromatic hydrocarbon ratios and NO<sub>x</sub> concentrations in the rural  
913 troposphere - observation of air-mass photochemical aging and NO<sub>x</sub> removal, *Atmos. Environ.*, 18,  
914 2421-2432, doi:10.1016/0004-6981(84)90012-x, 1984.



- 915 Russell, P. B., Bergstrom, R. W., Shinozuka, Y., Clarke, A. D., DeCarlo, P. F., Jimenez, J. L.,  
916 Livingston, J. M., Redemann, J., Dubovik, O., and Strawa, A.: Absorption Angstrom Exponent in  
917 AERONET and related data as an indicator of aerosol composition, *Atmos. Chem. Phys.*, 10, 1155-  
918 1169, doi:10.5194/acp-10-1155-2010, 2010.
- 919 Schnaiter, M., Linke, C., Mohler, O., Naumann, K. H., Saathoff, H., Wagner, R., Schurath, U.,  
920 and Wehner, B.: Absorption amplification of black carbon internally mixed with secondary organic  
921 aerosol, *J. Geophys. Res.-Atmos.*, 110, doi:10.1029/2005JD006046, 2005.
- 922 Schuster, G. L., Dubovik, O., and Holben, B. N.: Angstrom exponent and bimodal aerosol size  
923 distributions, *J. Geophys. Res.-Atmos.*, 111, D07207, doi:10.1029/2005JD006328, 2006.
- 924 Schwartz, S. E.: The whitehouse effect—Shortwave radiative forcing of climate by  
925 anthropogenic aerosols: an overview, *J. Aerosol Sci.*, 27, 359-382, doi:10.1016/0021-8502(95)00533-1,  
926 1996.
- 927 Schwarz, J. P., Gao, R. S., Fahey, D. W., Thomson, D. S., Watts, L. A., Wilson, J. C., Reeves, J.  
928 M., Darbeheshti, M., Baumgardner, D. G., Kok, G. L., Chung, S. H., Schulz, M., Hendricks, J., Lauer,  
929 A., Karcher, B., Slowik, J. G., Rosenlof, K. H., Thompson, T. L., Langford, A. O., Loewenstein, M.,  
930 and Aikin, K. C.: Single-particle measurements of midlatitude black carbon and light-scattering aerosols  
931 from the boundary layer to the lower stratosphere, *J. Geophys. Res.-Atmos.*, 111, D16207,  
932 doi:10.1029/2006jd007076, 2006.
- 933 Seinfeld, J. H. and Pandis, S. N.: *Atmospheric chemistry and physics : from air pollution to*  
934 *climate change*, Wiley, New York, 1998.
- 935 Setyan, A., Song, C., Merkel, M., Knighton, W. B., Onasch, T. B., Canagaratna, M. R.,  
936 Worsnop, D. R., Wiedensohler, A., Shilling, J. E., and Zhang, Q.: Chemistry of new particle growth in  
937 mixed urban and biogenic emissions – insights from CARES, *Atmos. Chem. Phys.*, 14, 6477-6494,  
938 doi:10.5194/acp-14-6477-2014, 2014.
- 939 Setyan, A., Zhang, Q., Merkel, M., Knighton, W. B., Sun, Y., Song, C., Shilling, J. E., Onasch,  
940 T. B., Herndon, S. C., Worsnop, D. R., Fast, J. D., Zaveri, R. A., Berg, L. K., Wiedensohler, A.,  
941 Flowers, B. A., Dubey, M. K., and Subramanian, R.: Characterization of submicron particles influenced  
942 by mixed biogenic and anthropogenic emissions using high-resolution aerosol mass spectrometry:  
943 results from CARES, *Atmos. Chem. Phys.*, 12, 8131-8156, doi:10.5194/acp-12-8131-2012, 2012.
- 944 Shilling, J. E., Zaveri, R. A., Fast, J. D., Kleinman, L., Alexander, M. L., Canagaratna, M. R.,  
945 Fortner, E., Hubbe, J. M., Jayne, J. T., Sedlacek, A., Setyan, A., Springston, S., Worsnop, D. R., and  
946 Zhang, Q.: Enhanced SOA formation from mixed anthropogenic and biogenic emissions during the  
947 CARES campaign, *Atmos. Chem. Phys.*, 13, 2091-2113, doi:10.5194/acp-13-2091-2013, 2013.



- 948 Tsigaridis, K., Daskalakis, N., Kanakidou, M., Adams, P. J., Artaxo, P., Bahadur, R., Balkanski,  
949 Y., Bauer, S. E., Bellouin, N., Benedetti, A., Bergman, T., Berntsen, T. K., Beukes, J. P., Bian, H.,  
950 Carslaw, K. S., Chin, M., Curci, G., Diehl, T., Easter, R. C., Ghan, S. J., Gong, S. L., Hodzic, A., Hoyle,  
951 C. R., Iversen, T., Jathar, S., Jimenez, J. L., Kaiser, J. W., Kirkevåg, A., Koch, D., Kokkola, H., Lee, Y.  
952 H., Lin, G., Liu, X., Luo, G., Ma, X., Mann, G. W., Mihalopoulos, N., Morcrette, J. J., Müller, J. F.,  
953 Myhre, G., Myriokefalitakis, S., Ng, N. L., O'Donnell, D., Penner, J. E., Pozzoli, L., Pringle, K. J.,  
954 Russell, L. M., Schulz, M., Sciare, J., Seland, Ø., Shindell, D. T., Sillman, S., Skeie, R. B., Spracklen,  
955 D., Stavrakou, T., Steenrod, S. D., Takemura, T., Tiitta, P., Tilmes, S., Tost, H., van Noije, T., van Zyl,  
956 P. G., von Salzen, K., Yu, F., Wang, Z., Wang, Z., Zaveri, R. A., Zhang, H., Zhang, K., Zhang, Q., and  
957 Zhang, X.: The AeroCom evaluation and intercomparison of organic aerosol in global models, Atmos.  
958 Chem. Phys., 14, 10845-10895, doi:10.5194/acp-14-10845-2014, 2014.
- 959 Virkkula, A., Ahlquist, N. C., Covert, D. S., Arnott, W. P., Sheridan, P. J., Quinn, P. K., and  
960 Coffman, D. J.: Modification, calibration and a field test of an instrument for measuring light absorption  
961 by particles, Aerosol Sci. Technol., 39, 68-83, doi:10.1080/027868290901963, 2005.
- 962 Wang, W., Rood, M. J., Carrico, C. M., Covert, D. S., Quinn, P. K., and Bates, T. S.: Aerosol  
963 optical properties along the northeast coast of North America during the New England Air Quality  
964 Study - Intercontinental Transport and Chemical Transformation 2004 campaign and the influence of  
965 aerosol composition, J. Geophys. Res.-Atmos., 112, D10S23, doi:10.1029/2006JD007579, 2007.
- 966 Warneke, C., de Gouw, J. A., Edwards, P. M., Holloway, J. S., Gilman, J. B., Kuster, W. C.,  
967 Graus, M., Atlas, E., Blake, D., Gentner, D. R., Goldstein, A. H., Harley, R. A., Alvarez, S.,  
968 Rappenglueck, B., Trainer, M., and Parrish, D. D.: Photochemical aging of volatile organic compounds  
969 in the Los Angeles basin: Weekday-weekend effect, J. Geophys. Res.-Atmos., 118, 5018-5028,  
970 doi:10.1002/jgrd.50423, 2013.
- 971 Warneke, C., McKeen, S. A., de Gouw, J. A., Goldan, P. D., Kuster, W. C., Holloway, J. S.,  
972 Williams, E. J., Lerner, B. M., Parrish, D. D., Trainer, M., Fehsenfeld, F. C., Kato, S., Atlas, E. L.,  
973 Baker, A., and Blake, D. R.: Determination of urban volatile organic compound emission ratios and  
974 comparison with an emissions database, J. Geophys. Res.-Atmos., 112, D10S47,  
975 doi:10.1029/2006JD007930, 2007.
- 976 Yang, M., Howell, S. G., Zhuang, J., and Huebert, B. J.: Attribution of aerosol light absorption  
977 to black carbon, brown carbon, and dust in China – interpretations of atmospheric measurements during  
978 EAST-AIRE, Atmos. Chem. Phys., 9, 2035-2050, doi:10.5194/acp-9-2035-2009, 2009.
- 979 Zaveri, R. A., Shaw, W. J., Cziczo, D. J., Schmid, B., Ferrare, R. A., Alexander, M. L.,  
980 Alexandrov, M., Alvarez, R. J., Arnott, W. P., Atkinson, D. B., Baidar, S., Banta, R. M., Barnard, J. C.,



981 Beranek, J., Berg, L. K., Brechtel, F., Brewer, W. A., Cahill, J. F., Cairns, B., Cappa, C. D., Chand, D.,  
982 China, S., Comstock, J. M., Dubey, M. K., Easter, R. C., Erickson, M. H., Fast, J. D., Floerchinger, C.,  
983 Flowers, B. A., Fortner, E., Gaffney, J. S., Gilles, M. K., Gorkowski, K., Gustafson, W. I., Gyawali, M.,  
984 Hair, J., Hardesty, R. M., Harworth, J. W., Herndon, S., Hiranuma, N., Hostetler, C., Hubbe, J. M.,  
985 Jayne, J. T., Jeong, H., Jobson, B. T., Kassianov, E. I., Kleinman, L. I., Kluzek, C., Knighton, B.,  
986 Kolesar, K. R., Kuang, C., Kubátová, A., Langford, A. O., Laskin, A., Laulainen, N., Marchbanks, R.  
987 D., Mazzoleni, C., Mei, F., Moffet, R. C., Nelson, D., Obland, M. D., Oetjen, H., Onasch, T. B., Ortega,  
988 I., Ottaviani, M., Pekour, M., Prather, K. A., Radney, J. G., Rogers, R. R., Sandberg, S. P., Sedlacek, A.,  
989 Senff, C. J., Senum, G., Setyan, A., Shilling, J. E., Shrivastava, M., Song, C., Springston, S. R.,  
990 Subramanian, R., Suski, K., Tomlinson, J., Volkamer, R., Wallace, H. W., Wang, J., Weickmann, A.  
991 M., Worsnop, D. R., Yu, X. Y., Zelenyuk, A., and Zhang, Q.: Overview of the 2010 Carbonaceous  
992 Aerosols and Radiative Effects Study (CARES), *Atmos. Chem. Phys.*, 12, 7647-7687, doi:10.5194/acp-  
993 12-7647-2012, 2012.

994 Zelenyuk, A., Imre, D., Nam, E. J., Han, Y. P., and Mueller, K.: ClusterSculptor: Software for  
995 expert-steered classification of single particle mass spectra, *Int. J. Mass Spectrom.*, 275, 1-10,  
996 doi:10.1016/j.ijms.2008.04.033, 2008.

997 Zelenyuk, A., Yang, J., Choi, E., and Imre, D.: SPLAT II: An Aircraft Compatible, Ultra-  
998 Sensitive, High Precision Instrument for In-Situ Characterization of the Size and Composition of Fine  
999 and Ultrafine Particles, *Aerosol Sci. Technol.*, 43, 411-424, doi:10.1080/02786820802709243, 2009.

1000 Zhang, Q., Jimenez, J. L., Canagaratna, M. R., Ulbrich, I. M., Ng, N. L., Worsnop, D. R., and  
1001 Sun, Y. L.: Understanding atmospheric organic aerosols via factor analysis of aerosol mass  
1002 spectrometry: a review, *Anal. Bioanal. Chem.*, 401, 3045-3067, doi:10.1007/s00216-011-5355-y, 2011.

1003

1004

1005

1006 **Table 1.** Table of instrumentation.

| <b>Instrument</b>   | <b>Property Measured</b>  | <b>Site</b> |
|---|---|-------------|
| UCD Photoacoustic Spectrometer (PAS) <sup>a</sup>                               | Dry PM <sub>2.5</sub> light absorption at 405 nm and 532 nm   | T0          |
| UCD Cavity Ringdown Spectrometer (CRDS) <sup>a</sup>                            | Dry PM <sub>2.5</sub> light extinction at 405 nm and 532 nm; humidified particle extinction at 532 nm                           | T0          |
| Particle Soot Absorption Photometer (PSAP) <sup>b</sup>                         | Dry PM <sub>1</sub> and PM <sub>10</sub> light absorption at 470, 532 and 660 nm  | T0, T1      |
| Nephelometer <sup>b</sup>   | Dry PM <sub>1</sub> and PM <sub>10</sub> light scattering at 450, 550 and 700 nm  | T0, T1      |
| Aerodyne High Resolution Time of Flight Aerosol Mass Spectrometer (HR-ToF-AMS)  | Non-refractory PM <sub>1</sub> composition (NR-PM <sub>1</sub> ); Organic aerosol types through positive matrix factor analysis | T0, T1      |
| PNNL Single Particle Laser Ablation Time of Flight Mass Spectrometer (SPLAT-II) | Single particle composition and identification for PM <sub>0.05</sub> -PM <sub>2</sub> (optimized for PM <sub>0.1-0.6</sub> )   | T0          |
| Particle Ablation Laser-desorption Mass Spectrometer (PALMS)                    | Single particle composition and identification for PM <sub>0.15</sub> -PM <sub>2</sub>  | T1          |
| Single Particle Soot Photometer (SP2)   | Refractory black carbon (rBC) number and mass concentration and size distributions  | T0, T1      |
| Scanning mobility particle sizer (SMPS)   | PM <sub>1</sub> particle mobility size distributions  | T0, T1      |
| Aerodynamic particle sizer (APS)  | PM <sub>0.7</sub> -PM <sub>10</sub> aerodynamic size distributions  | T0, T1      |
| NO <sub>x</sub> chemiluminescence   | NO + NO <sub>2</sub> (gas-phase)  | T0          |
| NO <sub>y</sub> by thermal conversion and chemiluminescence                     | Nitrogen oxides (NO + NO <sub>2</sub> + HNO <sub>3</sub> + alkyl nitrates + peroxy nitrates)                                    | T0          |
| Proton Transfer Reaction Mass Spectrometer (PTR-MS)                             | Concentrations of select volatile organic compounds (specifically, benzene and toluene)   | T0, T1      |

<sup>a</sup>These instruments sampled either ambient particles or particles that had been thermodenuded at 225 °C, switching on a 2.5 or 5 minute cycle

<sup>b</sup> These instruments alternately sampled PM<sub>1</sub> or PM<sub>10</sub> on a 6 minute cycle

1007

1008

1009 **Table 2.** Campaign average optical properties at T0 and T1 for submicron and supermicron particles.

| Property             | T0                    |                       |                          | T1                    |                          |
|----------------------|-----------------------|-----------------------|--------------------------|-----------------------|--------------------------|
|                      | PM <sub>1</sub>       | PM <sub>2.5</sub>     | supermicron <sup>+</sup> | PM <sub>1</sub>       | supermicron <sup>+</sup> |
| $b_{\text{sca},450}$ | 12.9 Mm <sup>-1</sup> |                       | 10.7 Mm <sup>-1</sup>    | 12.7 Mm <sup>-1</sup> | 6.6 Mm <sup>-1</sup>     |
| $b_{\text{sca},550}$ | 7.9 Mm <sup>-1</sup>  |                       | 10.9 Mm <sup>-1</sup>    | 7.6 Mm <sup>-1</sup>  | 6.8 Mm <sup>-1</sup>     |
| $b_{\text{sca},700}$ | 4.2 Mm <sup>-1</sup>  |                       | 10.9 Mm <sup>-1</sup>    | 3.4 Mm <sup>-1</sup>  | 6.8 Mm <sup>-1</sup>     |
| $b_{\text{abs},470}$ | 2.3 Mm <sup>-1</sup>  |                       | 0.31 Mm <sup>-1</sup>    | 1.45 Mm <sup>-1</sup> | 0.26 Mm <sup>-1</sup>    |
| $b_{\text{abs},530}$ | 1.9 Mm <sup>-1</sup>  |                       | 0.25 Mm <sup>-1</sup>    | 1.25 Mm <sup>-1</sup> | 0.20 Mm <sup>-1</sup>    |
| $b_{\text{abs},660}$ | 1.5 Mm <sup>-1</sup>  |                       | 0.19 Mm <sup>-1</sup>    | 0.95 Mm <sup>-1</sup> | 0.14 Mm <sup>-1</sup>    |
| $b_{\text{ext},405}$ |                       | 27.0 Mm <sup>-1</sup> |                          |                       |                          |
| $b_{\text{ext},532}$ |                       | 18.0 Mm <sup>-1</sup> |                          |                       |                          |
| $b_{\text{abs},405}$ |                       | 2.8 Mm <sup>-1</sup>  |                          |                       |                          |
| $b_{\text{abs},532}$ |                       | 2.1 Mm <sup>-1</sup>  |                          |                       |                          |
| $AAE_{470-532}^{\#}$ | 1.21 ± 0.18           |                       | 1.93 ± 0.83              | 1.22 ± 0.33           | 2.03 ± 1.04              |
| $AAE_{470-660}^{\#}$ | 1.17 ± 0.11           |                       | 1.54 ± 0.50              | 1.28 ± 0.22           | 1.76 ± 0.69              |
| $AAE_{532-660}^{\#}$ | 1.15 ± 0.12           |                       | 1.30 ± 0.52              | 1.28 ± 0.21           | 1.68 ± 0.77              |
| $AAE_{405-532}^{\#}$ |                       | 1.3 ± 0.9             |                          |                       |                          |
| $SAE_{450-550}^*$    | 2.42 ± 0.38           |                       | -0.13 ± 0.31             | 2.58 ± 0.27           | -0.15 ± 0.34             |
| $EAE_{405-532}^*$    |                       | 1.53 ± 0.5            |                          |                       |                          |

<sup>+</sup> Values for supermicron particles are calculated as the difference between PM<sub>10</sub> and PM<sub>1</sub>.

<sup>#</sup> The reported uncertainties were determined from fitting a histogram of the observed values to a Gaussian distribution and are the 1σ spread.

<sup>\*</sup> The reported uncertainties are 1σ standard deviations.

1010

1011

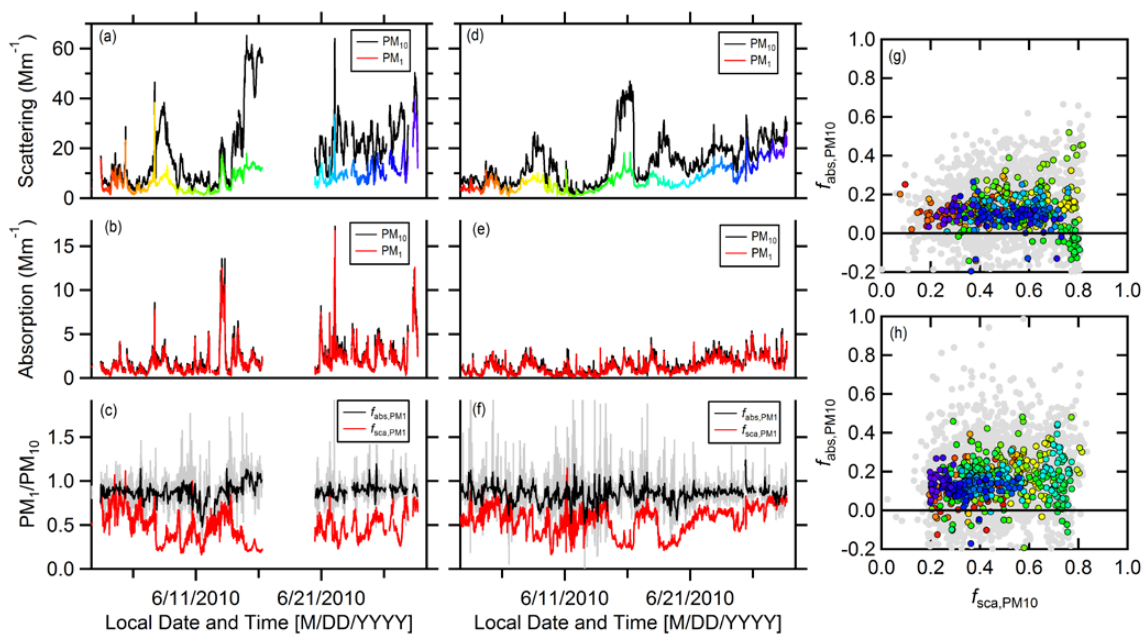
1012

1013

1014



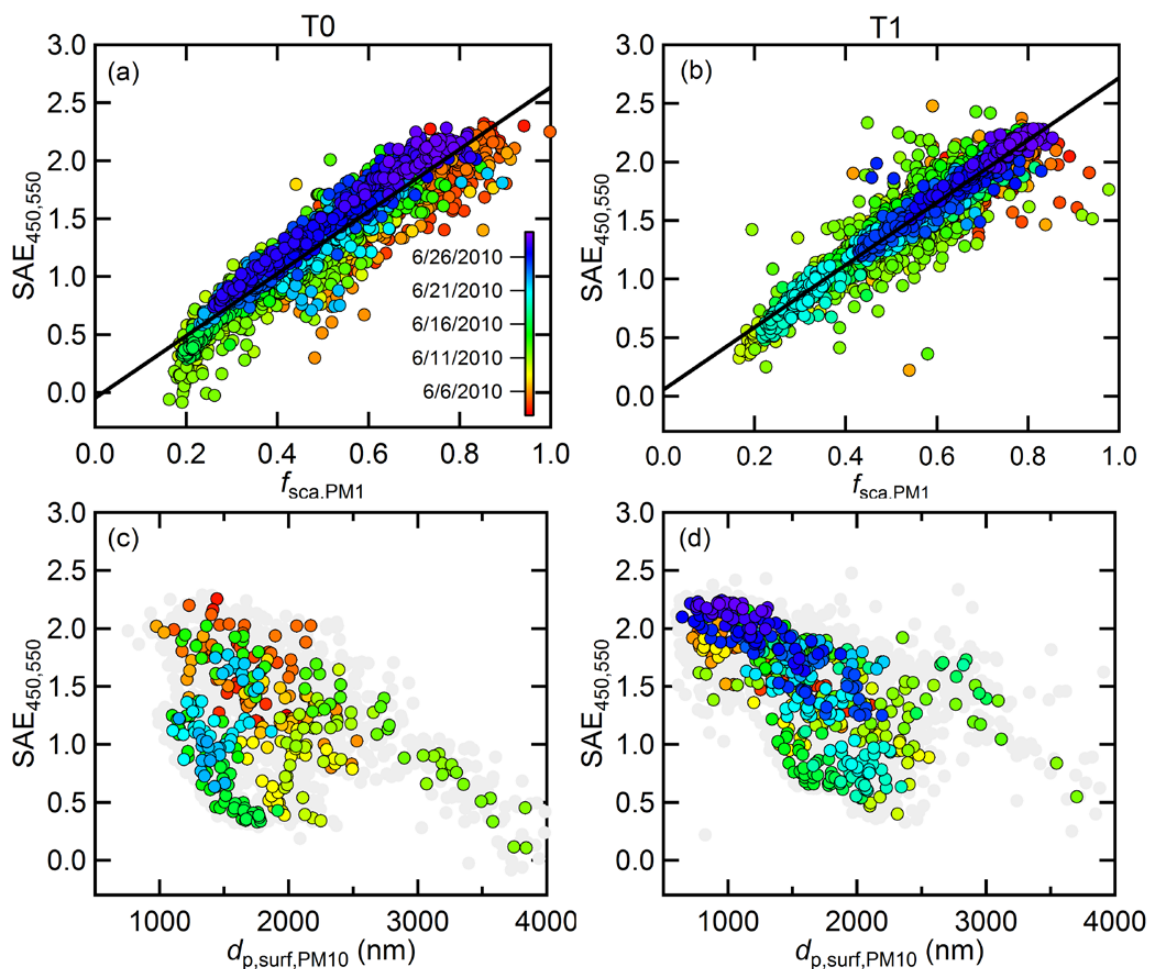
1015



1016

1017 **Figure 1.** Time-series of PM<sub>1</sub> and PM<sub>10</sub> scattering (a and d) and absorption (b and e) coefficients at 550  
 1018 nm for T0 (left panels) and T1 (right panels). Values for PM<sub>10</sub> are shown as black lines and for PM<sub>1</sub> as  
 1019 colored lines. The ratio between PM<sub>1</sub> and PM<sub>10</sub> scattering (red) and absorption (black) are shown in panels  
 1020 c and f. (For absorption, the data have been further averaged to 1 hour; the higher time resolution data are  
 1021 shown as gray.) The co-variation between  $f_{\text{abs,PM10}}$  and  $f_{\text{sca,PM10}}$  for T0 (g) and T1 (h) are also shown. The  
 1022 1-hr averaged points are colored according to time during the campaign, and correspond to the time-series  
 1023 in panels a and d; the gray points are the data at higher time-resolution.

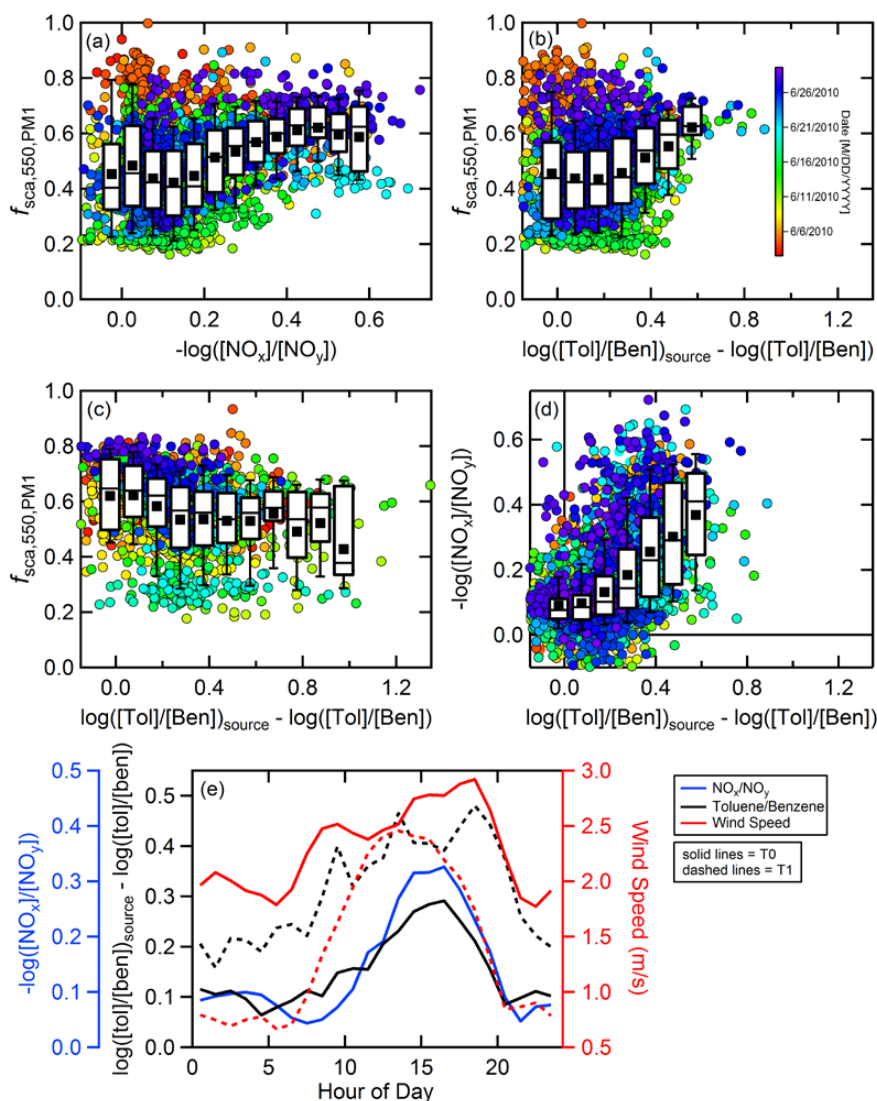
1024



1025

1026 **Figure 2.** (a,b) The relationship between the scattering Ångström exponent for the 450-550 nm pairs and  
1027 the  $f_{sca,PM1}$  for both T0 (left panels) and T1 (right panels). (c,d) The relationship between the SAE and the  
1028 median surface-weighted diameter for PM<sub>10</sub>. The points in all graphs are colored according to time during  
1029 the campaign (see legend). For panels (a,b) data at 10 min resolution are shown, while in panels (c,d) the  
1030 colored points are for data averaged to 1 h and the gray points are for 10 min data. The fewer colored  
1031 points in panel (c) is the result of a malfunction of the APS after 22 June 2010, which precludes calculation  
1032 of  $d_{p,surf,PM10}$ .

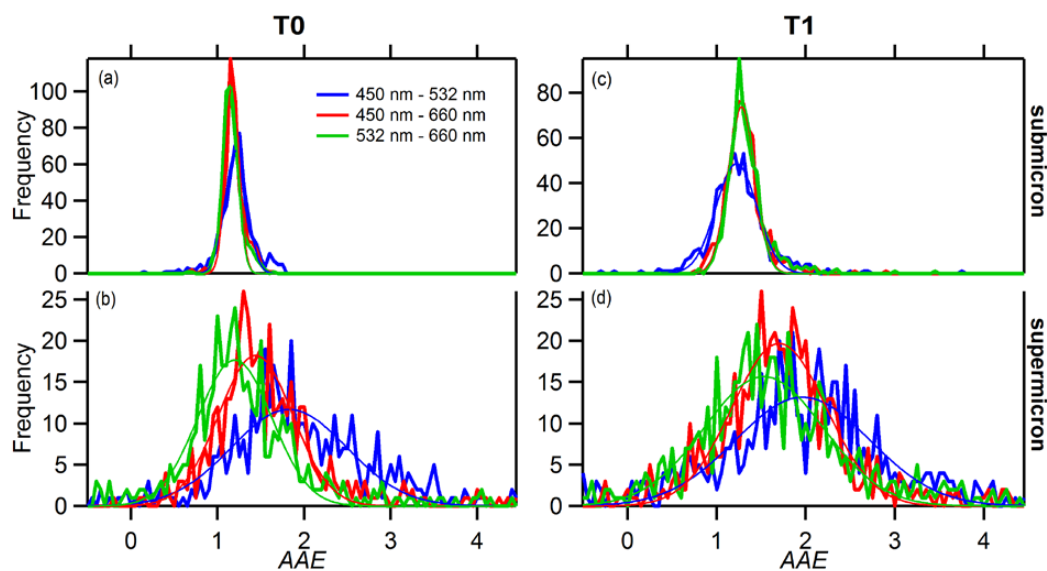
1033



1034

1035

1036 **Figure 3.** Submicron fraction of scattering for the T0 and T1 sites as a function of photochemical age  
 1037 proxies. Observations at T0 using the (a)  $NO_x/NO_y$  ratio and the (b) toluene/benzene ratio and at T1 for  
 1038 the (c) toluene/benzene ratio as the PCA proxy. Individual measurements (averaged to 10 minutes) are  
 1039 colored by time. (d) The relationship between the two PCA estimation methods at T0. (e) The diurnal  
 1040 variation in the PCA estimation methods and the measured wind speed for T0 (solid lines) and T1 (dashed  
 1041 lines). Box and whisker plots show the median (line), mean (square) upper and lower quartile (box) and  
 1042 10<sup>th</sup> and 90<sup>th</sup> percentile (whiskers).



1043

1044

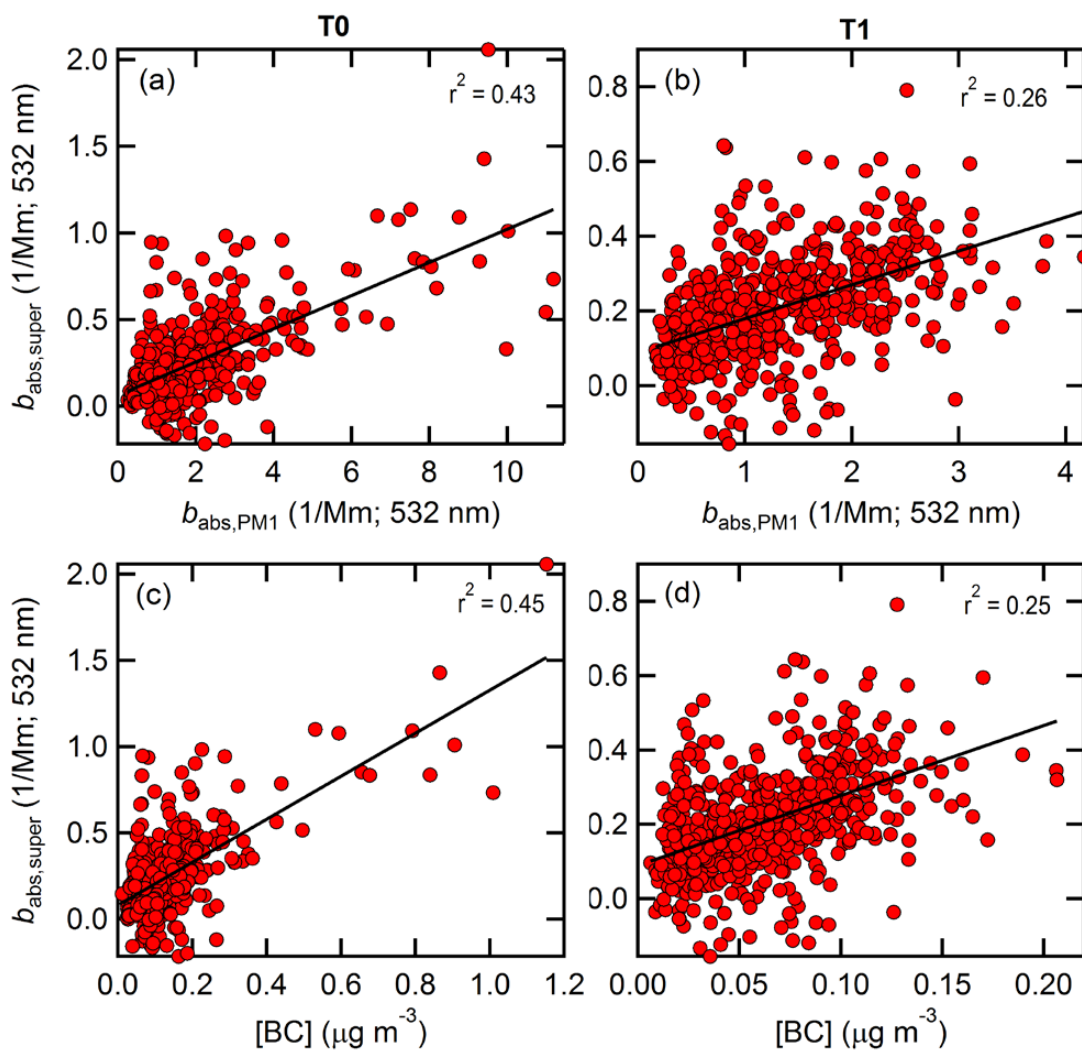
1045 **Figure 4.** Histograms of the measured AAE values for various wavelength pairs for submicron (top; a and  
1046 c) and supermicron (bottom; b and d) particles at the T0 (left) and T1 (right) sites. The different colors  
1047 correspond to different wavelength pairs (see legend). The thick lines correspond to the observations while  
1048 the thin lines show the results from fitting of the distributions to a Gaussian function.

1049



1050

1051

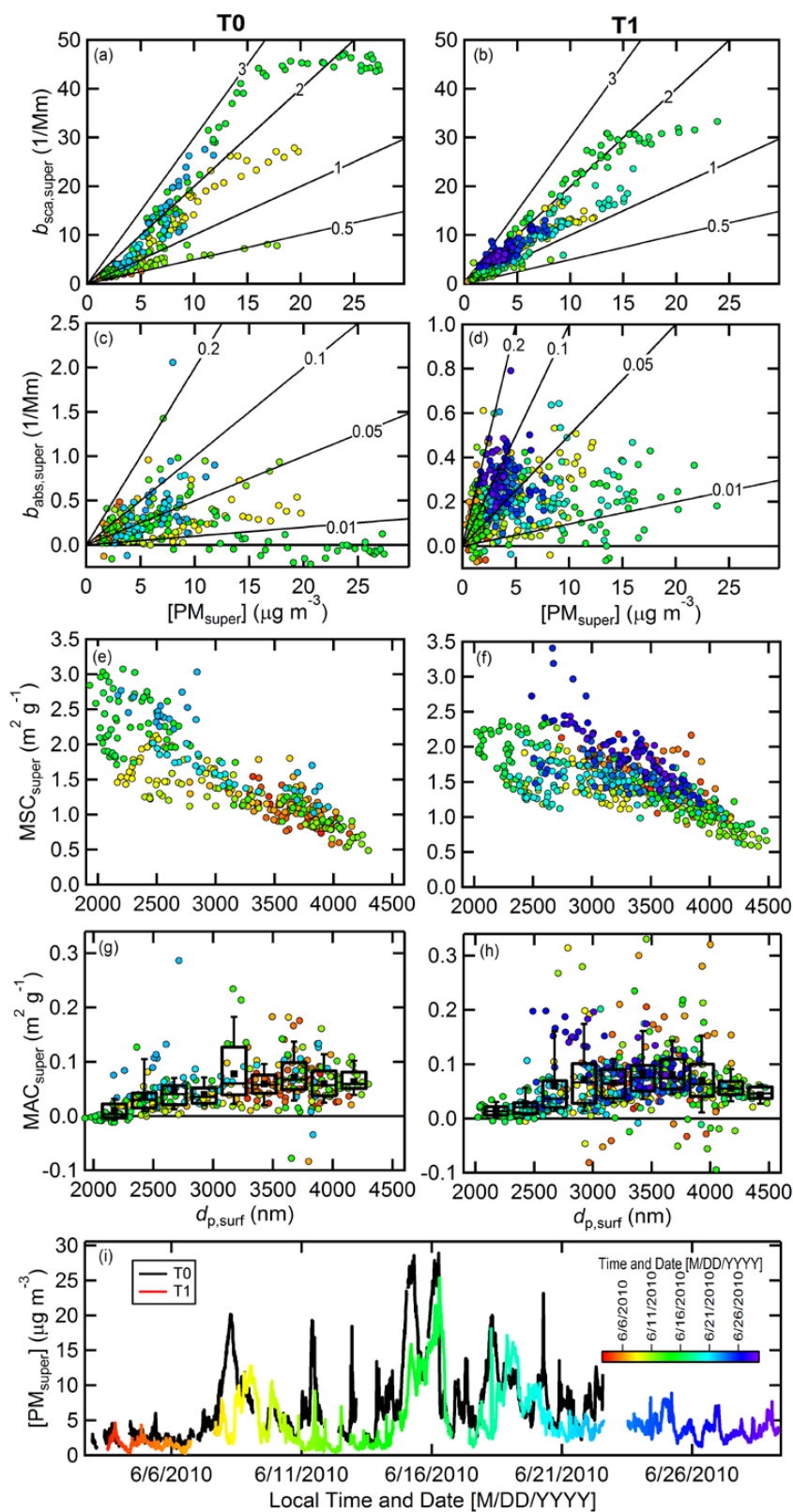


1052

1053

1054 **Figure 5.** Co-variation of the supermicron absorption at T0 (left panels) and T1 (right panels) with the  
1055 submicron absorption (top panels) and with black carbon concentration (bottom panels). Note that  
1056 negative values of  $b_{\text{abs,super}}$  result from this being derived from the difference between  $b_{\text{abs,PM10}}$  and  $b_{\text{abs,PM1}}$ .

1057

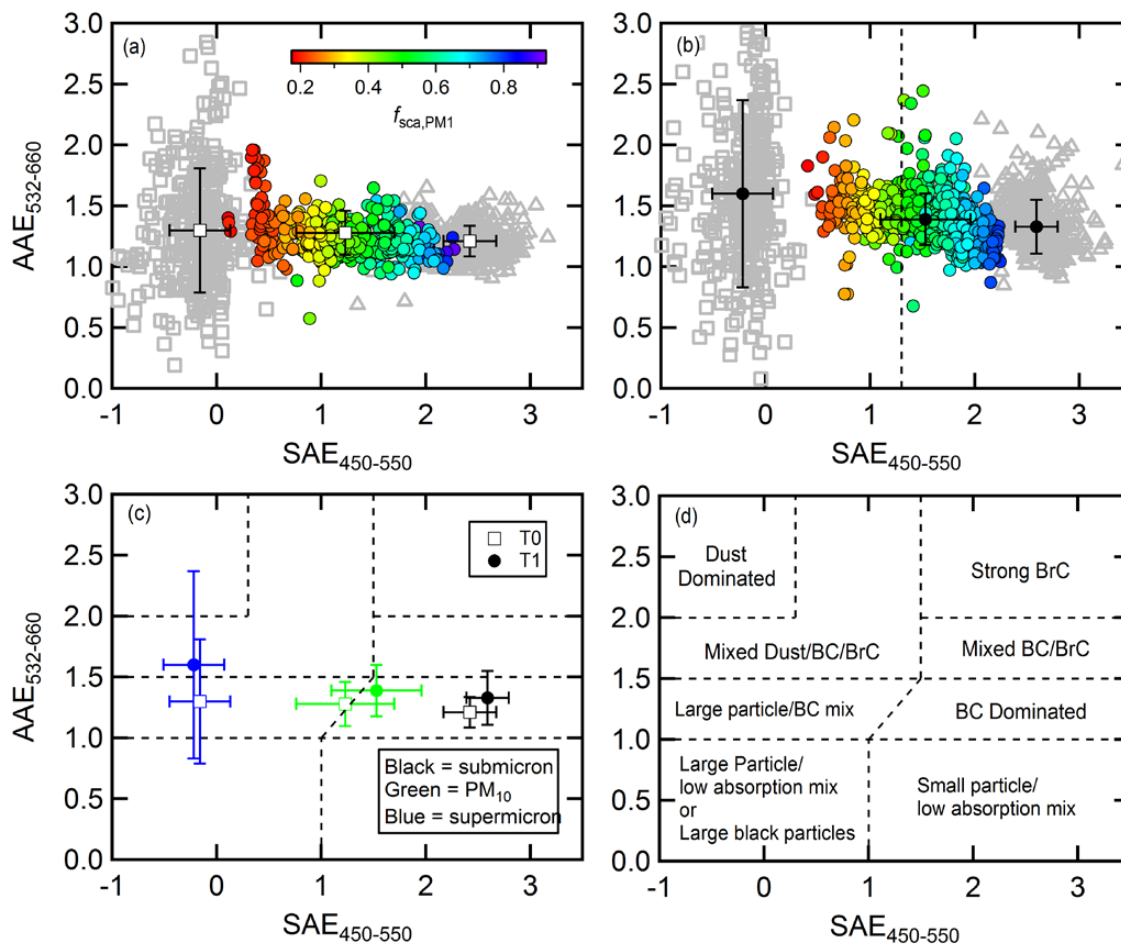




1059 **Figure 6.** (a,b) Scatter plot between  $b_{\text{sca,super}}$  at 532 nm and  $[\text{PM}_{\text{super}}]$  for (left panels) T0 and (right panels)  
1060 T1. The lines correspond to different  $MSC$  values (in  $\text{m}^2 \text{g}^{-1}$ ). (c,d) Scatter plot between  $b_{\text{abs,super}}$  at 532 nm  
1061 and  $[\text{PM}_{\text{super}}]$ . The lines correspond to different  $MAC$  values (in  $\text{m}^2 \text{g}^{-1}$ ). (e,f) The relationship between 1-  
1062 hr average  $MSC$  values and the surface area weighted mean diameter,  $d_{\text{p,surf}}$  at the two sites. (g,h) The  
1063 relationship between 1-hr average  $MAC$  values and  $d_{\text{p,surf}}$  at the two sites. The individual 1-hr average data  
1064 points are shown overlaid by box-and-whisker plots showing the mean (■), median (-), lower and upper  
1065 quartile (boxes), and 9<sup>th</sup> and 91<sup>st</sup> percentile (whiskers). The points in panels a-h are colored according to  
1066 time, and correspond to the colors in the bottom figure and color scale. (i) Time series of the supermicron  
1067 particle mass concentration for T0 and T1. T0 values are black lines, and T1 values are colored according  
1068 to time.

1069

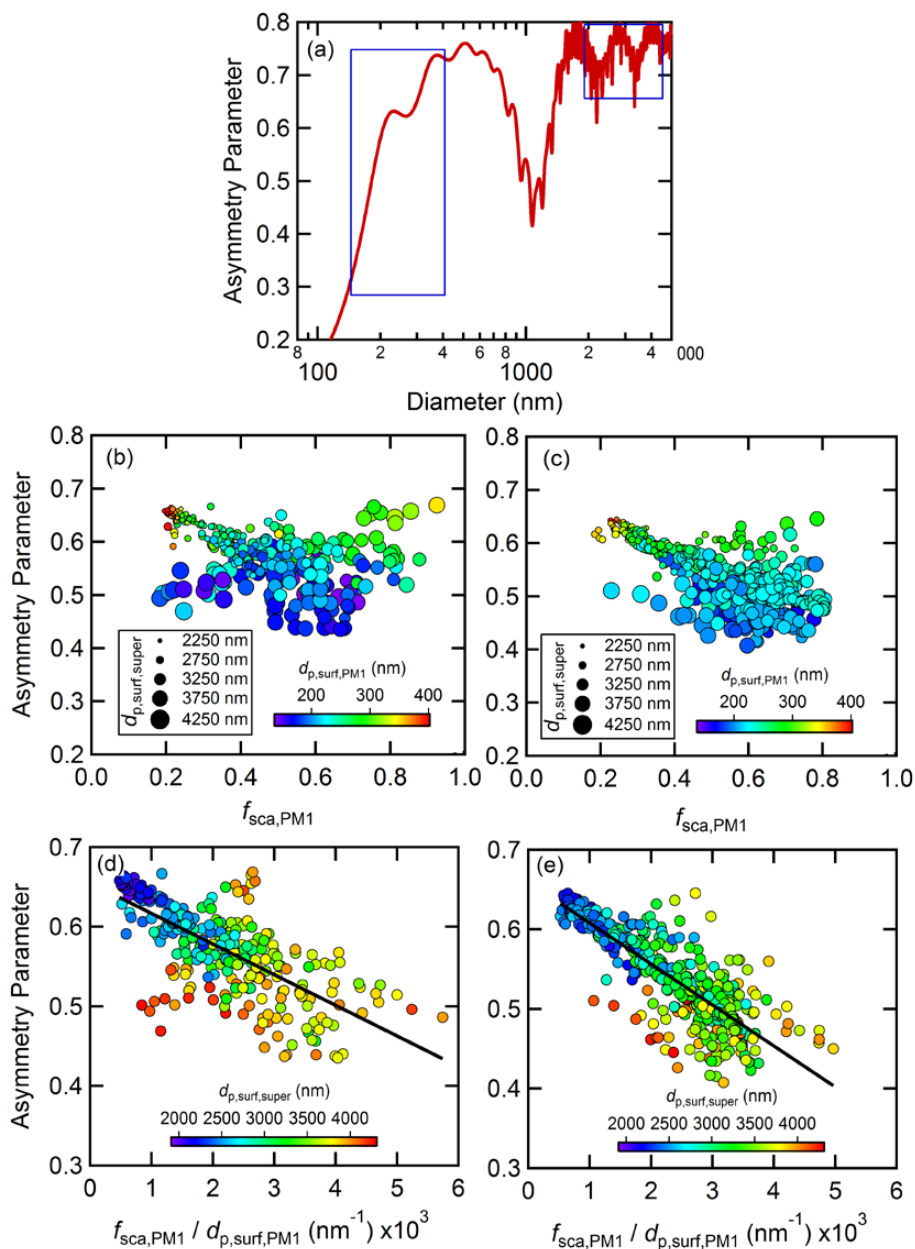
1070



1071

1072 **Figure 7.** Observed relationship between the AAE (532-600 nm pair) and the SAE (450-550 nm pair) for  
 1073 PM<sub>10</sub> (colored circles), submicron (open grey triangles) and supermicron (open grey squares) particles  
 1074 for the (a) T0 and (b) T1 sites. (c) Comparison between the PM<sub>10</sub> (green), submicron (black) and  
 1075 supermicron (blue) particle averages between the T0 (filled circles) and T1 (open squares) sites. (d) An  
 1076 alternate classification scheme to that suggested by Cazorla et al. (2013).

1077

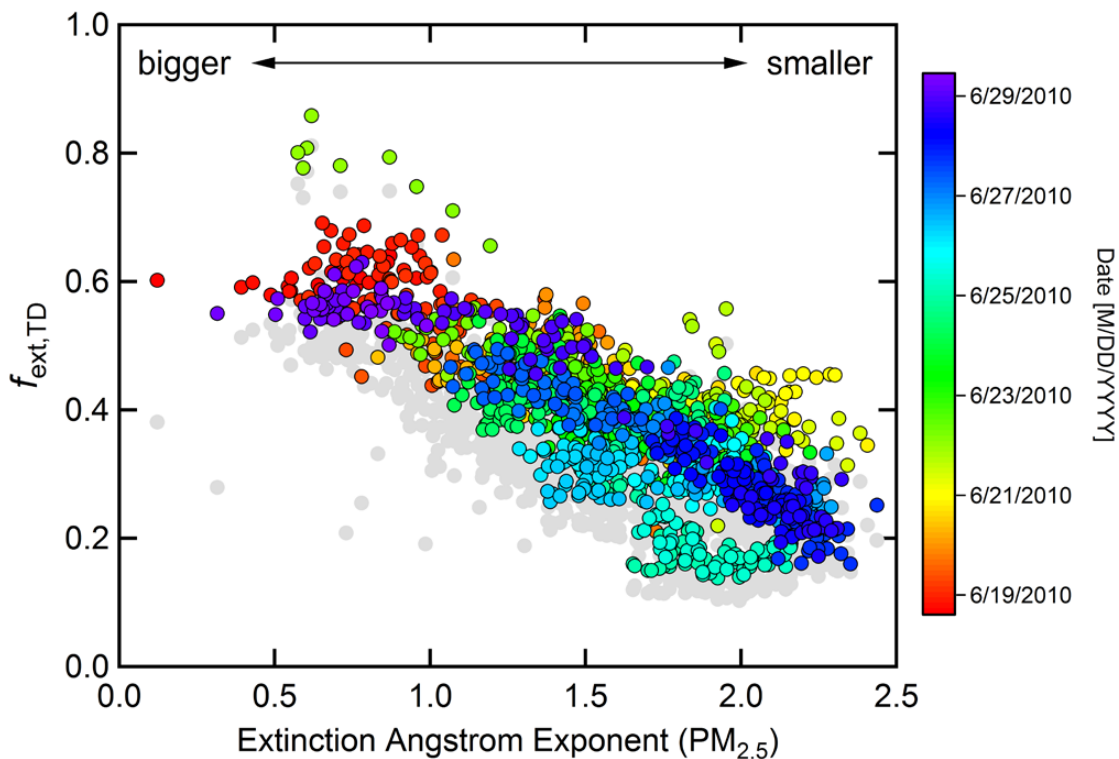


1078

1079 **Figure 8.** (a) Theoretical variation in the asymmetry parameter,  $g_{sca}$ , with particle diameter, assuming  
 1080 spherical particles with  $RI = 1.5 + 0.0i$ . The blue boxes indicate the range of  $d_{p,surf}$  values observed for  
 1081 submicron and supermicron particles. (b,c) The observed dependence of  $g_{sca}$  on  $f_{sca,PM1}$  for (b) T0 and (c)  
 1082 T1. The points are colored according to  $d_{p,surf,PM1}$  and the point size corresponds to  $d_{p,surf,super}$ . (d,e) The  
 1083 relationship between  $g_{sca}$  and  $R_g = f_{sca,PM1} / d_{p,surf,PM1}$  for (d) T0 and (e) T1. The points are colored  
 1084 according to  $d_{p,surf,super}$ .



1085

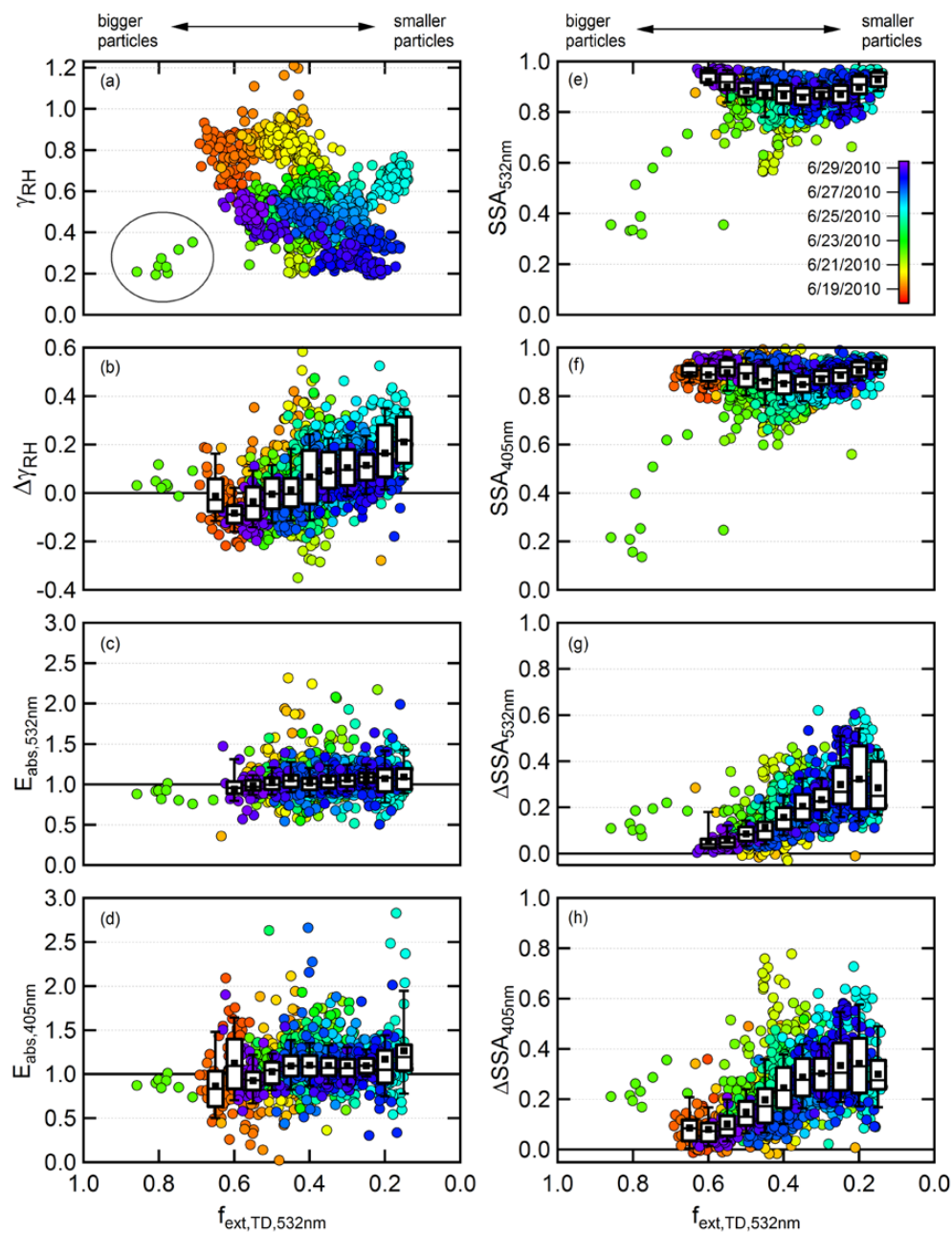


1086

1087 **Figure 9.** Variation of the extinction fraction remaining at 532 nm (colored points) and 405 nm (gray  
1088 points) as a function of the observed ambient particle extinction Ångstrom exponent for  $PM_{2.5}$ . The points  
1089 are colored by date.

1090

1091



1092  
 1093

**Figure 10.** Dependence of various intensive parameters on the fraction of extinction remaining after heating in the thermodenuder. Data are shown for (a) the absolute  $\gamma_{RH}$ , (b) the change in  $\gamma_{RH}$  (c) the absorption enhancement at 532 nm, (d) the absorption enhancement at 405 nm, (e) the SSA at 532 nm, (f) the SSA at 405 nm, (g) the change in SSA at 532 nm and (h) the change in SSA at 405 nm. The points are colored by time. The circled points in (a) show the period that was impacted by local road resurfacing activities.

1097  
 1098